batteries

MDPI

Article

Thermo-Electro-Mechanical Modeling and Experimental Validation of Thickness Change of a Lithium-Ion Pouch Cell with Blend Positive Electrode

David Schmider * and Wolfgang G. Bessler

Institute of Sustainable Energy Systems (INES), Offenburg University of Applied Sciences, Badstraße 24, 77652 Offenburg, Germany; wolfgang.bessler@hs-offenburg.de
* Correspondence: david.schmider@hs-offenburg.de

Abstract: Lithium-ion battery cells exhibit a complex and nonlinear coupling of thermal, electrochemical, and mechanical behavior. In order to increase insight into these processes, we report the development of a pseudo-three-dimensional (P3D) thermo-electro-mechanical model of a commercial lithium-ion pouch cell with graphite negative electrode and lithium nickel cobalt aluminum oxide/lithium cobalt oxide blend positive electrode. Nonlinear molar volumes of the active materials as function of lithium stoichiometry are taken from literature and implemented into the open-source software Cantera for convenient coupling to battery simulation codes. The model is parameterized and validated using electrical, thermal and thickness measurements over a wide range of C-rates from 0.05 C to 10 C. The combined experimental and simulated analyses show that thickness change during cycling is dominated by intercalation-induced swelling of graphite, while swelling of the two blend components partially cancel each other. At C-rates above 2 C, electrochemistry-induced temperature increase significantly contributes to cell swelling due to thermal expansion. The thickness changes are nonlinearly distributed over the thickness of the electrode pair due to gradients in the local lithiation, which may accelerate local degradation. Remaining discrepancies between simulation and experiment at high C-rates might be attributed to lithium plating, which is not considered in the model at present.

Keywords: lithium-ion batteries; pouch cell; thermo-electro-mechanical modeling; P3D; thickness change; blend electrode; Cantera

Citation: Schmider, D.; Bessler, W.G. Thermo-Electro-Mechanical Modeling and Experimental Validation of Thickness Change of a Lithium-Ion Pouch Cell with Blend Positive Electrode. *Batteries* **2023**, *9*, 354. https://doi.org/10.3390/batteries9070354

Academic Editors: Seung-Wan Song, Pascal Venet and Karim Zaghib

Received: 1 March 2023
Revised: 1 June 2023
Accepted: 13 June 2023
Published: 3 July 2023

1. Introduction

Lithium-ion batteries are the state-of-the-art technology for electrochemical energy storage used today in many stationary, mobile and portable applications [1]. Despite their high technological maturity, the lifetime of lithium-ion batteries is still limited. This poses problems for user acceptance, economic viability, and environmental sustainability [2,3]. Aging of lithium-ion batteries is caused by many different chemical and electrochemical mechanisms [4]. Research of the recent years has shown that mechanical effects also play a vital role and can cause severe ageing [4–6]. Changes in the crystal structures of the active materials (AM) during lithiation and delithiation cause alternating mechanical strains during cycling, leading to periodic thickness changes which are often described as cell "breathing" [7–9]. These intercalation-induced strains can lead to high stresses which ultimately lead to mechanical fatigue.

Physics-based modeling and simulation methods have proven excellent tools for understanding and further improving lithium-ion batteries [10–13]. They allow to study the processes occurring inside the battery cells and thus allow to derive measures to reduce cyclic and calendaric ageing [14]. Mechanical effects and electro-chemo-mechanical interactions can be included in physical models, which has been discussed in several review articles [5,6,15]. While the early works of Christensen and Newman [16], Zhang

et al. [16], and others [17–20] concentrated on describing the chemo-mechanical effects on the particle level, later work translated the particle expansion into the porous-electrode or even the cell levels [9,21–23]. This is not trivial, as the mechanical response of composite electrodes depends on multiple factors such as the constitution of the microstructure, the elastic properties and shape of the individual constituents, and the porosity. Gomadam and Weidner [24] derived a mathematical model to describe the interplay between particle and electrode expansion by a so-called swelling coefficient. This allows to accurately describe how much of the displacement introduced by the particles lead to a change in electrode dimension and how much is accommodated by the pore space and in turn decreases the porosity. However, this swelling coefficient is not known a priori and has to be elaborately determined experimentally. Rieger et al. [25] have correlated the relative thickness change of the porous electrode to the relative molar volume change of the AM particle, weighed by the AM volume fraction. This approach stands out for its relative simplicity. Although it uses a phenomenological relationship, it has been shown to provide good results when compared to experiments. Therefore, it was used in several other works [26–32].

In the present work we integrate the Rieger model into a multi-physics pseudo-three-dimensional (P3D) modeling framework developed and applied previously [33,34]. This framework particularly features the ability to accommodate blend electrodes and has been applied to cells both with positive electrode (PE) blends [34,35] and negative electrode (NE) blends [36]. We therefore generalize the Rieger approach to be applicable to electrodes with an arbitrary number of components. This results in a flexible thermo-electro-mechanical model, covering all relevant scales and physics to predict macroscopic dynamic current/voltage/temperature/thickness behavior. Required materials models and parameters are embedded in the flexible open-source software Cantera [37]. We demonstrate application to a high-power lithium-ion pouch cell with graphite NE and a blend lithium nickel cobalt aluminum oxide (NCA)/lithium cobalt oxide (LCO) PE. In the present work, we limit the study to the unconstrained cell expansion to model the cell breathing. In addition to the model development, the present work also features extensive experimental parameterization and validation of the simulation results.

With our work we aim to close the following gaps in the current state of research. (a) We generalize the Rieger approach to blend electrodes, that is, electrodes that contain more than one electrode material (here: blend NCA/LCO PE); (b) our framework includes a heat transport scale, which allows to predict cell temperature during cycling and therefore to analyze the individual contributions of intercalation-induced and thermal-induced cell expansion; (c) we enable the open-source code Cantera to consider non-ideal molar volumes. The article is structured as follows. Section 2 presents the experimental setup and the simulation methodology. Section 3 describes the parametrization approach using literature data and a thermal characterization experiment. Section 4 presents and discusses the results obtained with the combined modeling and experimental approach. Finally, the work is concluded in Section 5.

2. Materials and Methods

2.1. Investigated Cell

The cell investigated in this study is a commercial 350 mAh high-power lithium-ion pouch cell of the manufacturer Kokam (model number SLPB 283452H). The cell has a nominal voltage of 3.7 V and nominal charge and discharge cut-off voltages of 4.2 V and 3.0 V, respectively. Its cell chemistry was determined before to consist of a graphite NE and an NCA/LCO blend PE [38]. Furthermore, a P3D model of this cell, albeit without mechanical features, has been developed, parametrized and thoroughly validated by experiments [34], as well as applied to investigate overpotentials and partial impedance spectra [35] and the influence of electrode thickness on fast-charge capability [39]. For the present study, we have used an unused cell from the same batch and delivery as for the previous study [34]. This means that the cell had been resting for a total of 5 years after delivery. Although the cell was stored at low temperature (5–10 °C) and low SOC,

the results indicate moderate calendaric aging (10 mAh or 2.8% less capacity at 20 °C) as compared to the previous study [34]. This will be further discussed below.

2.2. Experimental Methodology

To investigate the cell swelling of the pouch cell we use an electrochemical dilatometry (ECD) setup [7]. ECD is a typical method for pouch cells that has been used extensively before [21,25,27,28,32,40–44]. Most of these literature examples use custom-made fixtures and parts. In contrast, we only use commercially available parts in order to keep the design effort comparatively low. Furthermore, this allows for easy reproduction of this experiment with the provided information about the used components. A simplified sketch and a photograph of our experimental setup is shown in Figure 1 and described hereafter.

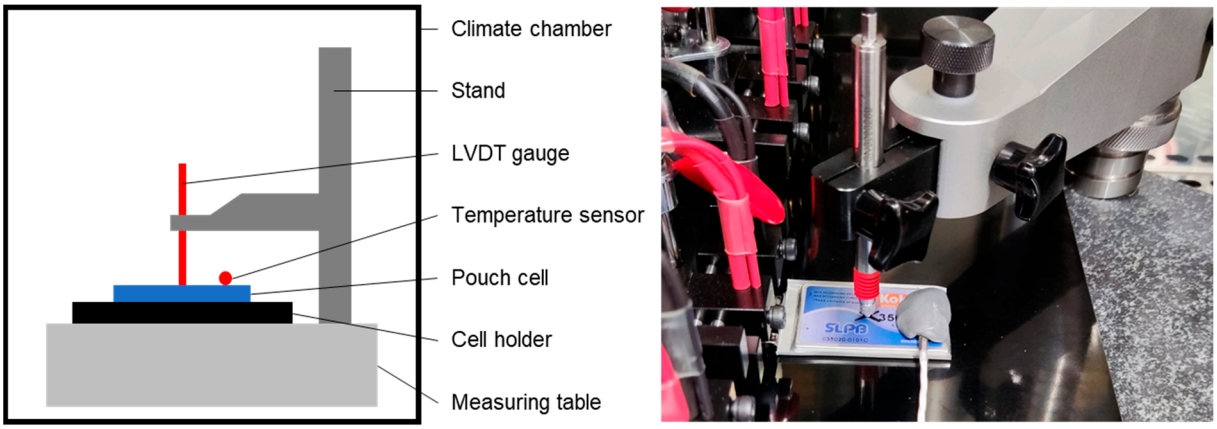

Figure 1. Schematic sketch (**left**) and photograph (**right**) of the experimental setup. LVDT, linear variable differential transformer.

The setup consists of a high precision measuring table with integrated stand (STEINLE HSF2520) and a pouch cell holder (BioLogic PBH-4). Experiments on the pouch cell were performed using a battery cycler (BioLogic VMP3 with 5 A Booster) while measuring the thickness perpendicular to the cell surface approx. in the cell center with a digital linear variable differential transformer (LVDT) gauge (Micro-Epsilon DTA-1G8-3-CA). The LVDT gauge has a measuring range of ±1 mm and a resolution of 0.24 µm. Due to the design, the accuracy of this type of sensor is best in the middle position of the measuring range, so the sensor was adjusted to that position at the beginning of the experiment. In addition, we record the cell surface temperature (BioLogic Pt-100). We assume the thickness change and temperature profile to be sufficiently uniform such that single-point measurements are justified [45]. The whole setup is kept at a constant ambient temperature of 20 °C inside a climate chamber (CTS -40/200 Li). Data post-processing and analysis was carried out in Matlab (R2019b).

We applied a conditioning protocol before the actual tests in order to establish proper contact between the cell and the LVDT gauge, to reduce irreversible displacement effects occurring in the first few cycles, and to drive the cell to a steady state after extended rest/storage. Unless stated otherwise, we applied a constant-current (CC) charge cut-off voltage of 4.2 V, a CC discharge cut-off voltage of 3.0 V, and constant-voltage (CV) cut-off currents of 0.0175 A (0.05 C). All C-rates given in this paper were calculated with respect to the nominal capacity of 350 mAh, that is, I = C-rate·0.35 Ah/1 h. After an initial constant-current constant-voltage (CCCV) discharge at 2 C and a consecutive resting phase of 0.5 h, the cell was charged and discharged with 2 C in a CCCV protocol for 20 cycles. One final CCCV charge/discharge cycle at 0.5 C was performed before a resting phase of 0.5 h. For the actual experiment we measured CCCV charge and discharge curves at five different C-rates of 0.05 C (0.0175 A), 1 C (0.35 A), 2 C (0.7 A), 5 C (1.75 A) and 10 C (3.5 A), respectively, each followed by a resting phase of 0.5 h. Although longer relaxation times

have also been reported in the literature for related experiments [45], we found that the measured quantities of interest (surface temperature and displacement) relax sufficiently within 0.5 h.

The maximum current of the battery cycler channel is ±5 A. For the lowest current of 17.5 mA (corresponding to 0.35% of the maximum cycler current, the cycler current accuracy is specified to be smaller than 10 mA) this resulted in minor inaccuracies (0.0473 mA difference between mean charge and discharge current) in the current measurement. Due to the long duration, these errors accumulate, leading to inconsistent calculations of charge throughput (charge vs. discharge). Therefore, the current measurement for 0.05 C was corrected such that the charge throughput of charge and discharge are equivalent. This correction was not applied to C-rates above 0.05 C.

For thermal characterization an additional experiment was performed using the same equipment. This is described in detail in Section 3.2.

2.3. Mechanical Model

For the present study we used and extended our existing P3D modeling and simulation framework, as well as an existing validated model of the Kokam pouch cell. The P3D modeling domain is shown in the Appendix A in Figure A1. It couples transport on three spatial scales (cell, electrode pair, particle), each described in one dimension (here denoted as x, y and z, respectively). The two lower scales are founded on the well-known "Newman"-type porous electrode models [46]. Additionally, our framework features the integration of detailed multi-step and/or multi-phase chemistries [13]. Details on the underlying governing equations, parameterization and implementation are elaborately described in previous works [33,34,47]. For this paper to be self-consistent, we give a full description of the physicochemical model in the Appendix A. In the following we focus on the derivation and integration of the mechanical model.

In this work we extended the base model to capture mechanical interactions inside the cell on the mesoscopic (electrode pair) and macroscopic (cell) scales, while the microscopic (particle) scale remains without mechanical model. The goal is to predict the cyclic expansion and contraction of the cell that is observed during operation. This is caused by three effects which will be addressed in the following and included in the model. The first effect is mechanical strain $\varepsilon_{\text{mech}}$. It is described by Hooke's law of linear elasticity in a one-dimensional representation as [48]

$$\varepsilon_{\text{mech}} = \frac{\Delta L_{\text{mech}}}{L^0} = \frac{\sigma_{\text{n}}}{E} \tag{1}$$

Here, ΔL_{mech} is the mechanical displacement with respect to the initial length L^0, σ_{n} is the normal stress and E is Young's modulus. We assume that the cell can expand freely so no normal stress builds up. This is realized by using the boundary condition [48]

$$\sigma_{\text{n}} = 0 \tag{2}$$

The second swelling effect is the thermal expansion ε_{th}, which is material-specific and formulated as [48]

$$\varepsilon_{\text{th}} = \frac{\Delta L_{\text{th}}}{L^0} = \alpha_{\text{th}} \Delta T \tag{3}$$

where ΔL_{th} is the thermal displacement, based on the initial length L^0, α_{th} is the thermal expansion coefficient and ΔT is the temperature difference with regards to a reference temperature. In principle, each individual material comprising the cell exhibits a material-specific thermal expansion that should be considered. To simplify the model, we measure an effective thermal expansion coefficient for the whole cell. This is described in more detail in Section 3.2.

The last effect we consider in the mechanical model is intercalation-induced strain ε_{int} resulting from intercalation and/or deintercalation of lithium ions into the AM par-

ticles. This causes changes in the lattice structure and therefore in the particle molar volume. To what extent the individual volumetric strains of the AM particles propagate to the electrode pair scale (mesoscale) and in turn result in macroscopically-observable swelling/contraction is not trivial to describe. The particle volumetric strain could partially expand into the pores, thus reducing the porosity and displacing liquid electrolyte out of the pore space. Furthermore, particles are in contact with neighboring particles, binder and conductive additives, thus swelling increases contact forces and stress. Therefore, only a part of the volumetric particle strain may lead to geometric change of the cell. It has been shown before that the in-plane dimensions (i.e., parallel to the electrode/separator interface) do not change and only the thickness change (i.e., perpendicular to the electrode/separator interface) is significant [25]. Therefore, we assume the area of the pouch cell to remain constant and consider this as a one-dimensional problem in the thickness direction. This is consistent with the dimensions of the P3D model. To translate the particle strain into thickness strain we make use of a formulation first presented in the works of Rieger [26,45,49] and recently used in the paper of Ai et al. [28], given as

$$\varepsilon_{\text{int}} = \frac{\Delta L_{\text{int}}}{L^0} \approx \varepsilon^0_{\text{AM}} \cdot \frac{\Delta V_{\text{m,AM}}}{V^0_{\text{m,AM}}} \tag{4}$$

Here, ΔL_{int} is the intercalation-induced displacement with respect to the initial length L^0, $\varepsilon^0_{\text{AM}}$ is the initial AM volume fraction, and $\Delta V_{\text{m,AM}}$ is the change in molar volume based on the reference molar volume $V^0_{\text{m,AM}}$. This equation relates the microscopic volumetric strain of the AM particles to the mesoscopic thickness strain by the proportionality factor of the initial AM volume fraction. Note that the symbol ε is used for both, strain and volume fraction, albeit with different indices.

In an ideal solid solution, the particle molar volume would increase linearly with increasing lithium concentration. However, many AM exhibit non-ideal molar volumes [50]. Thus, in our model we consider the volumetric strain $\Delta V_{\text{m,AM}}/V^0_{\text{m,AM}}$ to be a nonlinear function of lithium stoichiometry.

In order to solve the P3D model framework, the transport equations on each scale are discretized using a finite-volume approach. This offers a convenient way to integrate the mechanical model into the P3D model. For every finite volume k on the mesoscale (electrode pair, y scale) we combine the three Equations (1), (3) and (4) to solve for the length change ΔL_k,

$$\Delta L_k = \left(\frac{\sigma_{\text{n}}}{E_k} + \alpha_{\text{th},k} \Delta T + \sum_{j=1}^{N_{\text{AM}}} \varepsilon^0_{j,k} \cdot \frac{\Delta V_{\text{m},j,k}}{V^0_{\text{m},j,k}} \right) \cdot L^0_k \tag{5}$$

The mesoscale covers the complete electrode pair except for the current collectors (see Appendix A, Figure A1). Thus, ΔL_k describes the displacement of finite-volume elements within PE, separator or NE, depending on the index k starting with 1 at the PE/current collector interface (PE: $1 \leq k \leq 8$, separator: $9 \leq k \leq 15$, NE: $16 \leq k \leq 23$; corresponding discretization used in this work, cf. also Section 2.4). In the separator region, there is obviously no AM, thus the intercalation-induced term in Equation (5) is zero. Furthermore, because of the free expansion boundary condition in Equation (2), the separator is limited to thermal displacement, whereas PE and NE can expand thermally and due to intercalation. Since for blend electrodes multiple AM are combined, the sum j runs over the number of AM, N_{AM}, present in each finite volume. The total displacement of the electrode pair ΔL_{EP} is then the sum over all finite volumes N_{FV} according to

$$\Delta L_{\text{EP}} = \sum_{k=1}^{N_{\text{FV}}} \Delta L_k \tag{6}$$

The displacement of the complete cell ΔL_{cell} is given as the displacement of the electrode pair multiplied by the number of electrode pairs in the cell N_{EP},

$$\Delta L_{\text{cell}} = N_{\text{EP}} \cdot \Delta L_{\text{EP}} \tag{7}$$

The calculated length changes in each compartment are also used to update the discretized lengths in each solution step, thereby coupling the mechanical interactions to the transport equations. For further reference, the complete set of equations is given in the Appendix A.

The full P3D model couples electrochemical, thermal and mechanical behavior as follows. Electrochemistry is modeled temperature-dependent using Arrhenius type rate laws. Transport in the electrolyte is modeled temperature-dependent and also dependent on the electrode thicknesses. The temperature change of the cell is modeled based on chemical and ohmic heat source terms, thus providing feedback to electrochemistry and transport. The thickness change of the electrodes is modeled both due to intercalation-based expansion and thermal expansion, again providing feedback to electrochemistry and transport. Still, there are interactions not included in the present model: (a) On the particle scale, particle expansion is not considered; (b) on the electrode pair scale, the interaction between mechanical pressure and electrochemistry (e.g., pressure-dependent thermodynamics and kinetics) is not considered; (c) on the cell scale, the heat transport parameters (thermal conductivity and heat capacity) are assumed independent of temperature. Modeling these interactions have to be subject of future studies.

2.4. Simulation Methodology

We implemented the extended P3D model described above and in the Appendix A in the in-house multiphysics software package DENIS [33] (Detailed Electrochemistry and Numerical Impedance Simulation). To solve the set of differential-algebraic equations (DAE) we used the implicit time-adaptive solver LIMEX [51,52]. As a discretization scheme for spatial derivatives, we applied the finite volume method. In comparison to the base model [34], we modified the number of non-equidistant control volumes to 10, 23 and 11 on the x, y and z scales, respectively (cf. Figure A1 for schematic representation of the individual scales). As before, the cell is still represented by one single electrode pair. The open-source chemical kinetics code Cantera [37] (version 2.6.0) was used for the thermodynamically consistent description of the cell chemistry and was coupled to the DENIS transport model via the chemistry source terms. The DENIS simulations were controlled via an interface to MATLAB (version 2019a), which was also used for data analysis and visualization. On a laptop computer with Intel i7 3.00 GHz processor and 32 GB of RAM, it took approx. 5 min of wall-clock time to simulate a CCCV charge and discharge cycle at 1 C rate.

2.5. Tabulated Molar Volumes in Cantera

We model the AM in Cantera using the *BinarySolutionTabulatedThermo* class that was developed by Mayur et al. [47]. It models the AM of a lithium-ion battery as a binary mixture of the lithiated species Li[AM] (indexed with 1 in the following) and the host material or vacancy species V[AM] (indexed with 2 in the following). This class was derived from the *IdealSolidSolnPhase* parent class and extends the functionality of this parent class such that the user can provide tabulated molar enthalpies and entropies as function of lithium stoichiometry to account for non-ideal species thermodynamics.

The *IdealSolidSolnPhase* parent class includes an ideal solid solution model of the constituent species in terms of molar volumes: Each species i in the phase is assumed to have constant partial molar volume $\overline{V}_i$ equal to its pure species molar volume $V^*_{\text{m},i}$. In an ideal binary solid solution phase the molar volume varies linearly between the pure species molar volumes,

$$V_{\text{m,AM}} = X_1 \cdot \overline{V}_1 + X_2 \cdot \overline{V}_2 = X_1 \cdot V^*_{\text{m},1} + X_2 \cdot V^*_{\text{m},2} \tag{8}$$

with X_1 and X_2 being the respective mole fractions of each species. Since in a binary mixture the mole fractions of both species must sum to unity,

$$X_1 + X_2 = 1 \tag{9}$$

We can also write Equation (8) as function of only one mole fraction,

$$V_{\mathrm{m,AM}} = X_1 \cdot V^*_{\mathrm{m},1} + (1 - X_1) \cdot V^*_{\mathrm{m},2} \tag{10}$$

In a real binary mixture, such as a typical intercalation material, the species interact with each other, leading to deviations from the ideal behavior and resulting in nonlinear dependencies of the molar volume as a function of composition [53,54]. The equation for the molar volume thus becomes

$$V_{\mathrm{m,AM}} = X_1 \cdot \overline{V}_1 + (1 - X_1) \cdot \overline{V}_2 \tag{11}$$

Note that both partial molar volumes $\overline{V}_1$ and $\overline{V}_2$ are functions of the composition. Within this work, we extended the functionality of the *BinarySolutionTabulatedThermo* class to accept tabulated molar volumes $V_{\mathrm{m,AM}}(X_1)$. This allows to consider arbitrary dependencies of the molar volume on lithium stoichiometry. The partial molar volumes are computed by numerical differentiation, making use of the Gibbs-Duhem equation (cf. Smith et al. [54] for detailed derivation),

$$\overline{V}_1 = V_{\mathrm{m,AM}} + (1 - X_1) \cdot \frac{\mathrm{d}V_{\mathrm{m,AM}}}{\mathrm{d}X_1} \tag{12}$$

$$\overline{V}_2 = V_{\mathrm{m,AM}} - X_1 \cdot \frac{\mathrm{d}V_{\mathrm{m,AM}}}{\mathrm{d}X_1} \tag{13}$$

Additionally, the mass density of the phase is calculated as

$$\rho = \frac{X_1 \cdot M_1 + (1 - X_1) \cdot M_2}{V_{\mathrm{m,AM}}} \tag{14}$$

These extensions to the *BinarySolutionTabulatedThermo* class were implemented, reviewed and committed to the Cantera repository on GitHub, and merged into the main version with the release of stable version 2.6.0.

The table $V_{\mathrm{m,AM}}(X_1)$ needs to be provided by the user via the Cantera input file. Required values can be determined experimentally. In the context of lithium-ion battery AM, this is usually done by crystallographic X-ray diffraction (XRD) [55]. In these experiments, the lithium content in the AM is varied electrochemically while the lattice structure of the unit cell is characterized with XRD.

For the determination of the mechanical displacement as described in Section 2.3, we need to calculate $\frac{\Delta V_{\mathrm{m,AM}}}{V^0_{\mathrm{m,AM}}}$. Therefore, a defined reference $V^0_{\mathrm{m,AM}}$ is stored at the beginning of a simulation. $\Delta V_{\mathrm{m,AM}}$ is then computed in every solution step as

$$\Delta V_{\mathrm{m,AM}} = V_{\mathrm{m,AM}}(X_1) - V^0_{\mathrm{m,AM}} \tag{15}$$

where $V_{\mathrm{m,AM}}(X_1)$ is obtained from Cantera. Since lithium concentration gradients may occur in the particles at high current densities, particle averaged lithium mole fractions are used.

3. Model Parameterization

3.1. Volume Changes of Active Materials

The expansion of a lithium-ion battery electrode is caused by a change in the lattice structure of the AM during intercalation of lithium. A key parameter of the mechani-

cal model is therefore the relative molar volume change $\Delta V_{m,AM}/V^0_{m,AM}$ of the AM (cf. Equation (4)). As we did not perform material-specific experiments or calculations ourselves, we use data from literature, available from dilatometric studies or XRD experiments. The selected sources of XRD data including the corresponding primary sources are listed in Table 1. While graphite has been extensively studied, data sources for volume change of NCA and LCO are comparatively scarce in literature. Furthermore, not all sources cover the complete lithium stoichiometric range since the transition metal oxides become unstable towards lower lithium stoichiometries.

The relative molar volumes $V_{m,AM}/V^0_{m,AM}$ are visualized in Figure 2 as function of lithium stoichiometry X. Note that the relative molar volume $V_{m,AM}/V^0_{m,AM}$ and the relative molar volume change $\Delta V_{m,AM}/V^0_{m,AM}$ show the same trend and are connected as

$$\frac{\Delta V_{m,AM}}{V^0_{m,AM}} = \frac{V_{m,AM} - V^0_{m,AM}}{V^0_{m,AM}} = \frac{V_{m,AM}}{V^0_{m,AM}} - 1 \tag{16}$$

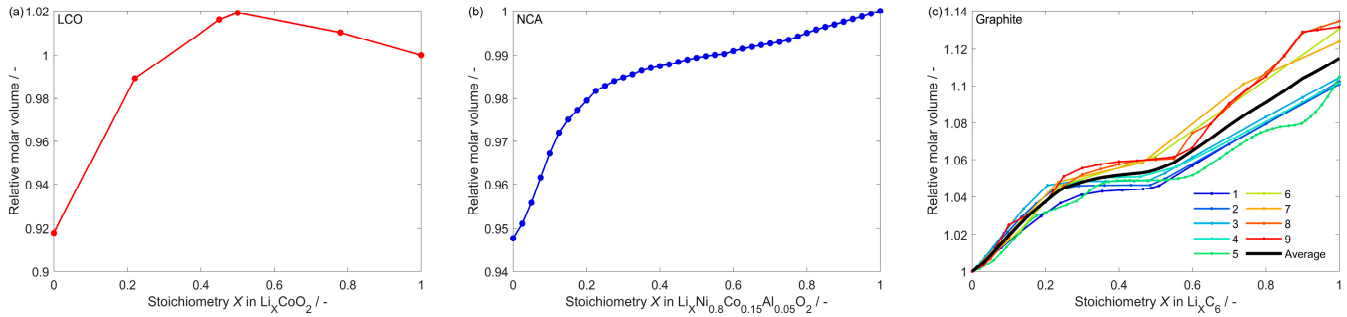

Figure 2. Relative molar volume $V_{m,AM}/V^0_{m,AM}$ as function of lithium stoichiometry X derived from published XRD experimental data for the three AM (**a**) LCO, (**b**) NCA and (**c**) graphite. For graphite, different data sources are compared. See Table 1 for references and text for details.

We intentionally plot the relative molar volume in Figure 2 since we need the molar volume as an input for Cantera, which can be easily calculated by multiplying by $V^0_{m,AM}$ (compare Figures 2 and A2 panel g–i). The lithium stoichiometry X is defined here as the lithium concentration relative to the maximum lithium concentration,

$$X = \frac{c_{Li}}{c_{max,Li}} \tag{17}$$

such that X can theoretically vary between 0 and 1. This can also be represented in the chemical formula, for example Li_XC_6 for graphite or Li_XCoO_2 for LCO. Note also that X is equal to X_1 introduced in Section 2.5. We furthermore use $V^0_{m,AM}$ at the chemically most stable stoichiometry, that is, $V_{m,AM}/V^0_{m,AM} = 1$ at $X = 0$ for graphite and at $X = 1$ for LCO and NCA. The values for $V^0_{m,AM}$ were computed as described in Mayur et al. [47] by

$$V^0_{m,AM} = \frac{M}{\rho} \tag{18}$$

with M being the molar mass of the fully delithiated species ($X = 0$) in case of graphite and the fully lithiated species ($X = 1$) for LCO and NCA. The reference densities ρ are taken from Ref. [38] and listed in Table A4. Thus, we get the following values: $V^0_{m,LCO} = 20.43\ cm^3/mol$; $V^0_{m,NCA} = 20.43\ cm^3/mol$; $V^0_{m,Graphite} = 31.75\ cm^3/mol$. By multiplying these $V^0_{m,AM}$ with the respective relative molar volume curves in Figure 2 we get the input molar volumes $V_{m,AM}(X_1)$ needed for Cantera (cf. Figure A2 panel g–i). Although we use these nonlinear curves, it is still possible to simulate ideal solid solution behavior by assuming linear variation as described in Section 2.5 between the limiting val-

ues at $X = 0$ and $X = 1$ (LCO: $V_{m,X=0} = 18.75\ cm^3/mol$, $V_{m,X=1} = 20.43\ cm^3/mol$; NCA: $V_{m,X=0} = 23.35\ cm^3/mol$, $V_{m,X=1} = 20.43\ cm^3/mol$; Graphite: $V_{m,X=0} = 31.75\ cm^3/mol$, $V_{m,X=1} = 35.40\ cm^3/mol$).

Usually, the AM expand with increasing lithium stoichiometry. LCO (Figure 2a), however, shows an inverted behavior and expands in the beginning of delithiation. In fully lithiated LCO the lithium interstitials screen the Coulombic repulsion between the layers. As lithium is removed during deintercalation, the Coulombic repulsion increases and leads to an expansion. This effect has been investigated and discussed before in detail [50,56–59]. In NCA (Figure 2b), on the other hand, the molar volume increases monotonously with increasing lithiation. It is therefore possible that the swelling of LCO and NCA in the blend PE cancel each other out, depending on the stoichiometry ranges. This will be further discussed in Section 4.3. Graphite (Figure 2c) expands considerably more than the other AM, exhibiting a relative volume change of over 10% over the complete range of lithiation. Hence, it may be expected that the swelling of the investigated cell is largely determined by graphite. The nine different sources of XRD data of graphite show a significant scatter of $V_{m,AM}/V^0_{m,AM}$ in the range of 1.10 to 1.13 at $X = 1$. In literature, different test conditions as well as graphite compositions, and resulting differences in microstructure and crystallinity, are reported as probable reasons for the observed scatter [26,60]. In order to compare the influence of the different data on the simulation output, we carried out simulations of a full charge and discharge cycle at 0.05 C for every individual parameter set. Figure 3 shows a comparison of the resulting displacement curves, including the experimental data, as function of time. All simulations agree qualitatively with the experiments, but a significant scatter of the data is obvious. The experimental measurements are approximately in between the different simulations. We therefore use the arithmetic average of all nine sources as input parameter for all further simulations.

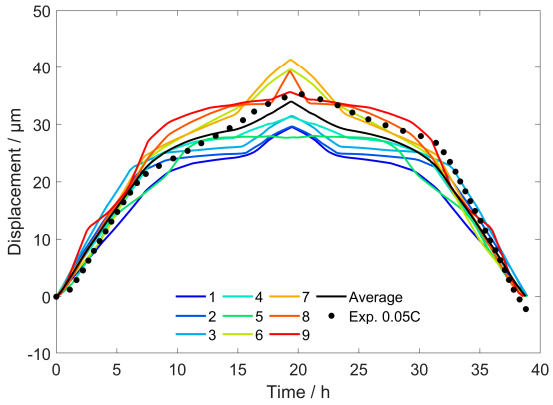

Figure 3. Simulated displacement of the lithium-ion pouch cell as function of time for a 0.05 C cycle (first charge, then discharge) for different literature parameters of the graphite relative molar volume (Figure 2c), compared to the experimental measurement. The numbers indicated in the legend correspond to the references listed in Table 1.

It should be noted that in LCO, not the complete X range is practically accessible, as the material decomposes below $X \approx 0.5$ [61]. However, Amatucci et al. [56] were able to characterize the lattice structure of the fully delithiated end member (CoO_2) of LCO by XRD experiments. Thus, data for the complete lithium stoichiometric range of LCO, is available as displayed in Figure 2a.

Table 1. Literature sources of XRD data of intercalation-induced volume changes.

Material	Source	Primary Source	Comment
Graphite			
1	Ref. [26] Figure 2a, Curve 1	[62,63]	Calculated in [26] from average d-spacing
2	Ref. [26] Figure 2a, Curve 2	[64,65]	Calculated in [26] from average d-spacing
3	Ref. [26] Figure 2a, Curve 3	[65,66]	Calculated in [26] from average d-spacing
4	Ref. [26] Figure 2a, Curve 4	[67]	Calculated in [26] from average d-spacing
5	Ref. [26] Figure 2a, Curve 5	[65,68]	Calculated in [26] from average d-spacing
6	Ref. [40] Table A1	[69,70]	
7	Ref. [32] Figure 3a	[71]	Average of charge and discharge
8	Ref. [55] Table S1, 2nd cycle	-	Average of charge and discharge, linearly extrapolated to $X = 1$
9	Ref. [55] Table S1, 3rd cycle	-	Average of charge and discharge, linearly extrapolated to $X = 1$
NCA			
	Ref. [72] Figure 3c	-	Average of charge and discharge
LCO			
	Ref. [73] Table 1	[56]	Outliers at $X = 0.9$ and $X = 0.51$ are not considered

3.2. Thermal Parameters

For the thermo-electro-mechanical model, a number of thermal parameters are required. This includes the effective thermal expansion coefficient α_{th} (cf. Equation (3)) and the convective heat transfer coefficient at the cell surface α_{surf}, both of which were obtained by dedicated experiments described in this Section. Further thermal parameters include effective heat conductivities, heat capacities, and activation energies of all chemical and transport parameters, which were taken unchanged from our previous work [34].

A thermal experiment similar to that used by Rieger et al. [26] was used to determine α_{th} and α_{surf}. The same test setup as described in Section 2.2 was used. To achieve a heating of the cell without invoking electrochemical expansion of the cell, the cell was rapidly cycled with alternating CC charge and discharge phases at a current of 10 C with a frequency of 1 Hz. The high currents lead to a heating of the cell, while the high frequency allows to keep the state of charge (SOC) approximately constant. Rieger et al. [26] showed that the SOC has no significant influence on the thermal expansion, therefore the experiments were only carried out at nominal 50% SOC. This was achieved by initially discharging the cell completely and then charging it to 50% of the nominal capacity of 350 mAh. After half an hour rest with the ambient temperature set to 20 °C, the rapid cycling protocol was applied until a surface temperature of 25 °C was reached, therefore increasing the temperature by 5 K. Then the cell was left to cool for another half an hour before the procedure was repeated. In total, five of such heating/cooling cycles were recorded. During the experiment we measured current, voltage, cell thickness and surface temperature.

An overview of the measured data during the experiment is shown in Figure 4. Panel a shows current and voltage as function of time. After the initial discharge/charge cycle up to 1 h, the data exhibit five distinct periods of rapid cycling, which appear as "blocks" because the curves are not resolved on the time scale shown in the figure. The open-circuit voltage during the following resting phases remains constant, indicating that the rapid

cycling does not change the SOC. Figure 4b shows cell surface temperature and thickness as function of time. Temperature rises during the rapid cycling phases up to 25 °C during approx. 222 s, followed by an exponential decay back to ambient temperature during the cooling phases. The thickness signal is clearly correlated to the temperature.

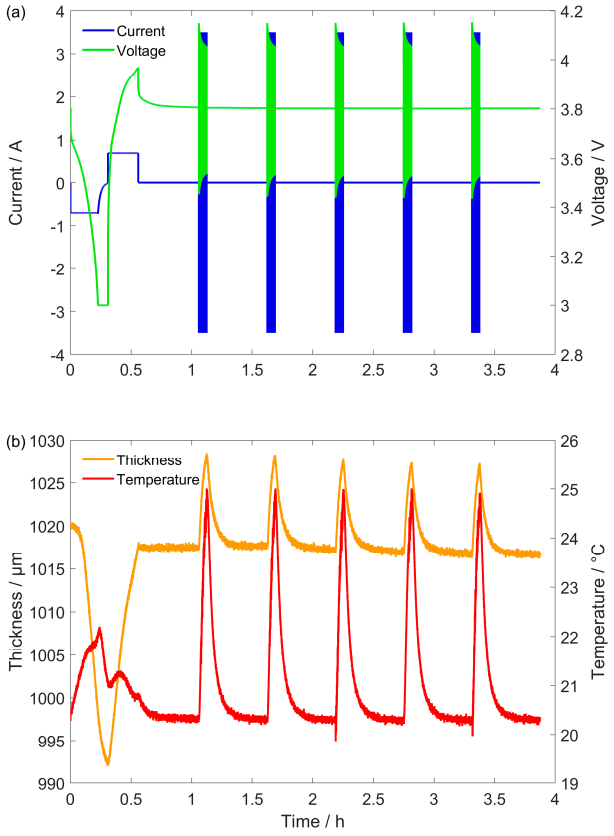

Figure 4. Rapid cycling experiment for thermal characterization. (**a**) Current (positive for charge) and voltage, (**b**) thickness and surface temperature as function of time.

For evaluation of α_{th}, the displacement during the cooling phases was plotted as function of the temperature difference $\Delta T = T_{\mathrm{surf}} - T_{\mathrm{amb}}$. These results are shown in Figure 5a. The data reveal a linear trend. The effective thermal expansion coefficient was obtained with a linear fit of each cooling phase data set and subsequently taking the average value of all five slopes, resulting in a mean value of 2.069 µm/K with a standard deviation of 0.067 µm/K. This value was divided by the number of 22 electrode pairs and the sum of the thickness of PE, NE and separator of 97.7 µm to yield the thermal expansion coefficient of $\alpha_{\mathrm{th}} = 9.63 \cdot 10^{-4}$ 1/K. The thermal expansion measured in the experiment also contains contributions of the current collectors. Since they are not discretized in the model, we only divide by the total length of the PE, separator and NE.

For the estimation of α_{surf}, we assume that the cell is thermally thin and can therefore be described with a lumped thermal capacity model [48]. This means that there is no significant temperature gradient inside the cell and the heat transfer can solely be described by an exponential surface convection equation,

$$\Delta T(t) = \Delta T_0 \cdot \exp\left(-\frac{\alpha_{\mathrm{surf}} \cdot A}{m \cdot c_p} \cdot t\right) \tag{19}$$

By applying the natural logarithm to this equation, a linear relationship is obtained,

$$\ln \Delta T(t) = \ln \Delta T_0 - \frac{\alpha_{\mathrm{surf}} \cdot A}{m \cdot c_p} \cdot t \tag{20}$$

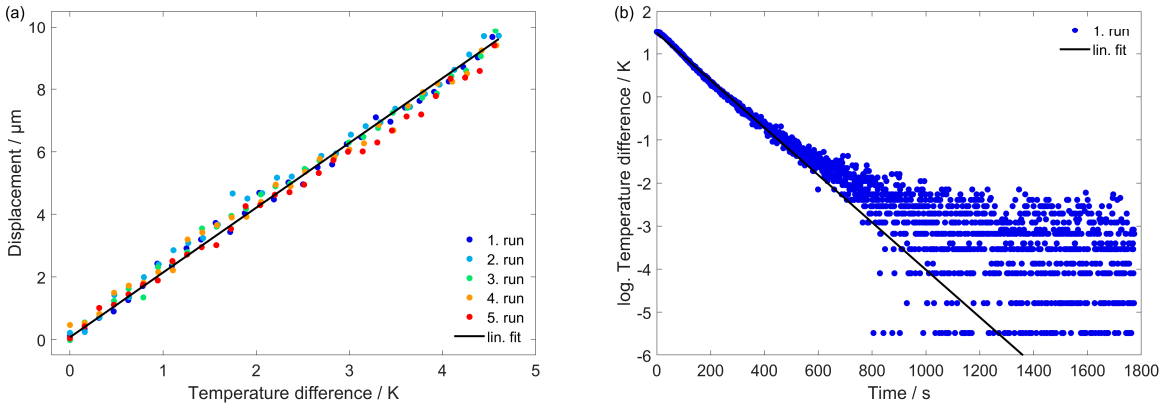

Figure 5. Identification of thermal parameters. (**a**) Displacement as function of temperature difference of the five consecutive cooling phases. For clarity, only 30 data points of each data set are shown. (**b**) Logarithmic temperature difference as function of time (exemplarily for the first of five cooling phases). The solid curves each show a linear fit. In panel (**a**) this linear fit shows the averaged slope of all five cooling phases.

The slope of a linear fit allowed to determine the heat transfer coefficient to a mean value of $\alpha_{\text{surf}} = 30.11\ \text{W}/(\text{m}^2\text{K})$ with a standard deviation of $0.58\ \text{W}/(\text{m}^2\text{K})$ (again averaged for all five cooling phases). Data are shown exemplarily for the first cooling phase in Figure 5b. Note that the linear fit is only applied for times $t < 450$ s, because the noise in the signal becomes more significant after this and in turn the signal deviates from its exponential characteristic. With the derived heat transfer coefficient and the thermal conductivity taken from the reference model, we furthermore performed a Biot number check to verify the assumption of a thermally thin cell [48]. The Biot number Bi was calculated as

$$Bi = \frac{\alpha_{\text{surf}} L}{\lambda} = \frac{30.11\,\frac{\text{W}}{\text{m}^2\text{K}} \cdot 0.003\ \text{m}}{0.9\,\frac{\text{W}}{\text{mK}}} = 0.1 \tag{21}$$

As $Bi = 0.1$, the cell is indeed thermally thin, thus confirming the assumption we make for determining α_{surf}.

With the thermal parameters available, we validated the full model by simulating the thermal experiment. We used the P3D model to carry out a virtual experiment with the identical protocol (bringing cell to 50% SOC, rapid 10 C cycling with 1 Hz until temperature reached 25 °C, rest for half an hour). In the present setup, the cell is placed on top of the plastic baseplate of the cell holder, such that the surface of the cell is directly exposed to the air cooling of the climate chamber. Therefore, we assumed convective heat flux boundary conditions at the top cell surface. We also assumed adiabatic boundary conditions at the bottom cell surface due to the low heat conductivity of thermoplastic materials. Figure 6 shows a comparison of the experimental results with the simulation, starting at the beginning of the first cooling phase. For both the displacement and the temperature the simulation shows a very good agreement with the experiment. Over the course of the five repetitions, an increasing time difference of peak temperature is visible between simulation and experiment. This is caused by a marginally steeper slope of the temperature rise in the simulation. Therefore, the model reaches 25 °C slightly earlier, which results in a shorter heating phase. Although this error is small, it accumulates with every repetition. Considering the long duration of the experiment, the delay can still be considered small. The P3D model was thus shown to be able to successfully reproduce thermo-electro-mechanical cell behavior.

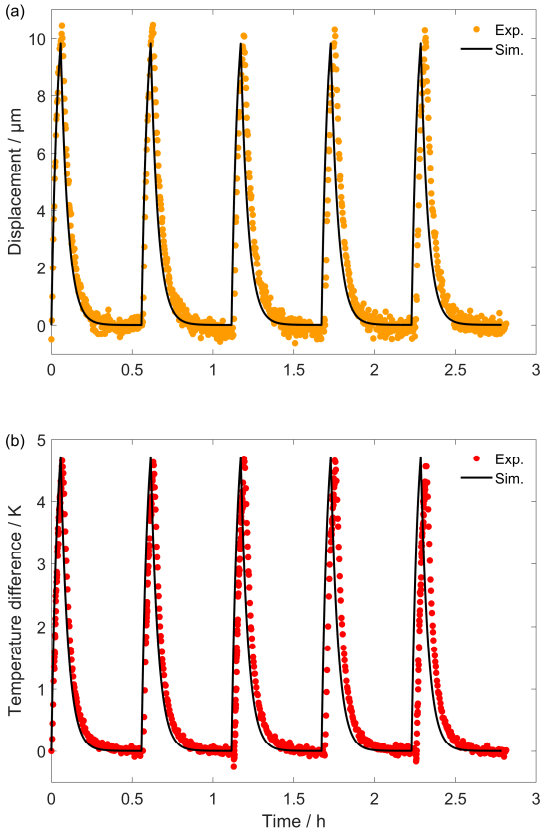

Figure 6. Rapid cycling experiment for thermal characterization: Comparison of simulation and experiment for (**a**) displacement and (**b**) temperature difference. Note that the time axis is set to zero at the beginning of the first heating phase.

3.3. Model Adjustment for Calendaric Ageing

As mentioned in Section 2.1, the investigated cell has aged since the parameterization for the base model [34]. We therefore adjusted the model parameters as follows. Changes in the electrode stoichiometry ranges were determined using our in-house electrode-balancer tool [38]. The resulting lithium stoichiometry ranges of the AM are given in Table A5 in the Appendix A. Furthermore, the temperature-dependent ohmic resistance was fitted to the recorded surface temperature profiles. This is based on the assumption that a higher internal resistance results in higher thermal losses. The fitting procedure results in an ohmic resistance of $R^0_{cc} = 7{\cdot}10^{-1}\mathrm{m\Omega{\cdot}m^2}$ and a slope of $\alpha_{cc} = -0.01$.

4. Results and Discussion

4.1. Thermo-Electrochemical Behavior

Figure 7 shows an overview of the measured current, voltage, displacement, and temperature during the full length of the experiment. The complete experiment took approx. 79 h, divided in about 32 h conditioning (indicated by the dashed vertical line in the figure) and 47 h of cycling. The current (panel a) follows the predefined protocol (cf. Section 2.2). The voltage (panel b) cycles between its upper and lower cut-off values of 4.2 V and 3.0 V, respectively. The thickness measurement (panel c) shows some irreversible variance in the beginning of conditioning, probably before proper contact between cell and measurement head is established. Already in this general overview, the typical "breathing" of the cell can be seen in an expansion during charge and a contraction during discharge. A more detailed analysis of the displacement will be given below. The temperature (panel d) stays almost constant during the low C-rate of 0.05 C. At higher C-rates the temperature increases more pronounced, peaking in approx. 32 °C at 10 C. In contrast to the thermal

characterization experiment (Section 3.2), where the cell self-heating was limited to 25 °C, temperature rise was not constrained during this cycling experiment.

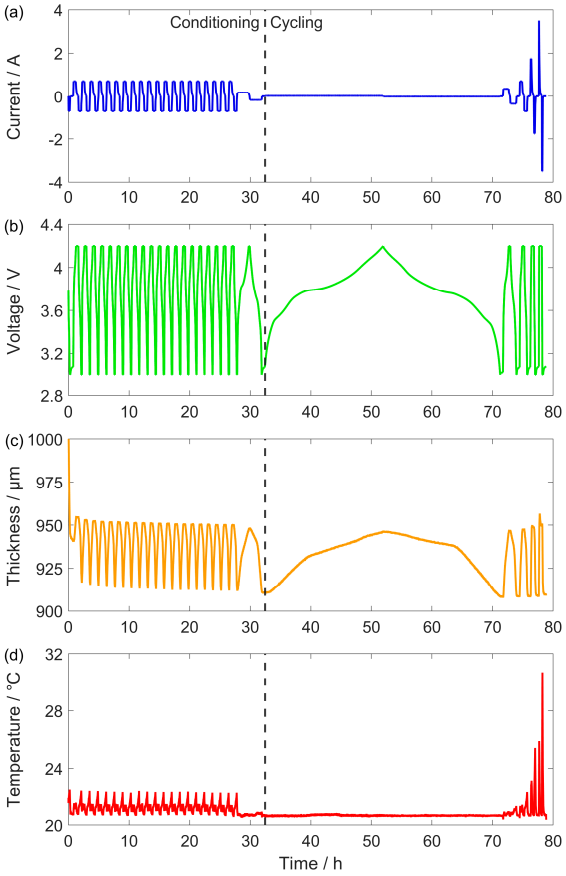

Figure 7. Overview of the experimental data. (**a**) Measured current (positive for charge), (**b**) voltage, (**c**) thickness, (**d**) temperature as function of time. The vertical dashed lines separate the conditioning protocol from the beginning of the actual cycling experiment.

In a virtual experiment, the parameterized P3D model was operated with the identical cycling protocol (without conditioning) as the experimental cell, using the applied current as input and predicting voltage, displacement, and temperature. Figure 8 shows a direct comparison between simulated and experimental voltage and temperature, which allows to assess the electro-thermal behavior, while the mechanical behavior will be discussed in more detail below. Panel a plots the charge and discharge voltage curves as function of the charge throughput. Panel b shows the temperature as function of normalized time; here, a value of zero is the start of charge and a value of one the end of discharge. These representations allow to compare the different C-rates in one plot despite the significant variation of the duration of the experiments from approx. 39 h at 0.05 C to approx. 43 min at 10 C. Note that the rest time is not included in the normalized time scale. The simulated voltage curves (panel a) show a good quantitative agreement with the experimental data. The increase in overpotential with increasing current, visible as increasing space between charge and discharge branches, is well reproduced, as is the onset and length of the CV phases. The simulated temperature curves (panel b) also show a very good agreement with the experiments. In particular, the increase of maximum temperature with increasing C-rate, the temperature asymmetry between charge and discharge, and the "fine structure" (slope changes, multiple peaks) of the temperature are reproduced.

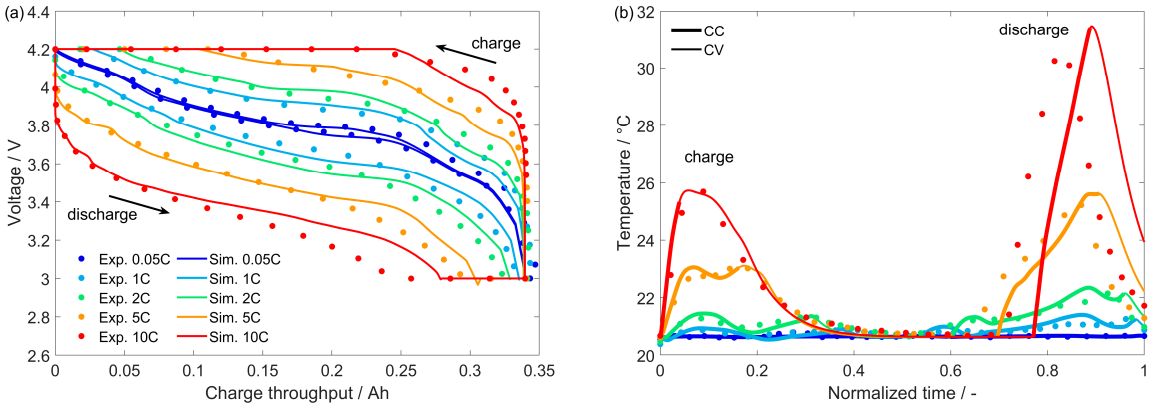

Figure 8. Experimental and simulated CCCV charge and discharge cycles at different C-rates. (**a**) Voltage as function of charge throughput and (**b**) cell surface temperature as function of normalized time. In panel (**a**), the lower branches represent discharge (time progressing from left to right) and the upper branches charge (time progressing from right to left), where the charge throughput of both, charge and discharge curves are normalized to a fully-charged cell. In panel (**b**), normalized time is defined as time after beginning-of-charge over time of end-of-discharge. The thick and thin parts of the solid lines represent the CC and CV phases, respectively.

In order to further quantify the accuracy of the simulation results, we have calculated the mean absolute error (MAE) between simulations and experiments as

$$\mathrm{MAE_V} = \sum_{i=1}^{N} \left| V_{\mathrm{sim},i} - V_{\mathrm{exp},i} \right| \mathrm{and} \mathrm{MAE_T} = \sum_{i=1}^{N} \left| T_{\mathrm{sim},i} - T_{\mathrm{exp},i} \right| \tag{22}$$

where, the sums run over one charge and discharge cycle with one point per second along the normalized time scale, and MAE were calculated individually for every C-rate. The resulting values are for $\mathrm{MAE_V}$: 0.01 V (0.05 C), 0.03 V (1 C), 0.04 V (2 C), 0.07 V (5 C), 0.09 V (10 C); and for $\mathrm{MAE_T}$: 0.03 K (0.05 C), 0.11 K (1 C), 0.16 K (2 C), 0.49 K (5 C), 1.29 K (10 C). The MAE confirms the trend that is visible in Figure 8: With higher C-rate, the error is increasing. It is worthwhile noting that all conditions were simulated with the identical model, that is, there were no parameter adaptions for different C-rates. The model accuracy observed here is typical for P2D and P3D models [33,34,46]. It is owed to the simplifications in the underlying model assumption, in particular, the homogenization on all three pseudo scales that ignores the significant structural complexities of particle shape, electrode microstructure, and cell design. In this light, the observed magnitude of the MAE can be considered rather small.

In conclusion, we can consider the thermo-electrochemical part of the model as valid over the complete investigated range of conditions.

4.2. Mechanical Behavior

Figure 9 shows the displacement for all C-rates for the experiment (panel a) and the simulation (panel b), plotted against normalized time. Upon charge (first half of data), the experimentally-observed displacement increases nonlinearly, its shape and maximum depending on C-rate. Upon discharge (second half of data), the displacement decreases again. The simulations agree qualitatively with the measurements. As will be further discussed below (Section 4.3), the behavior is dominated by the intercalation-induced swelling, in particular at low C-rates where the temperature is almost constant (cf. Figure 8b). With increasing C-rates, temperature increases more pronounced, thereby the influence of thermal expansion increases. This changes the overall shape of the displacement curves. The high peaks in surface temperature (cf. Figure 8b) at 5 C and 10 C lead to an "overshoot" in the displacement signal, which flattens during the cooldown at the CV phases. This behavior is seen in experiments as well as in simulations.

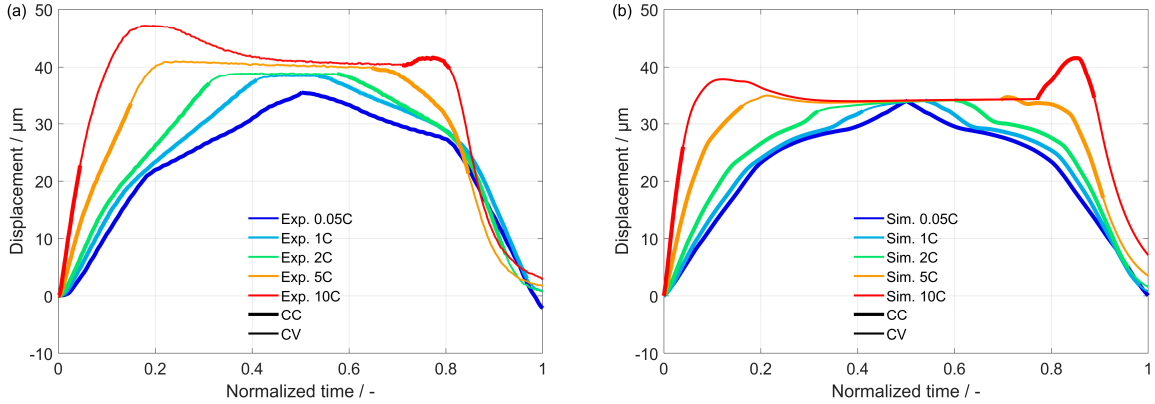

Figure 9. Experimental and simulated CCCV charge and discharge cycles at different C-rates. (**a**) Experimental displacement, (**b**) simulated displacement. Normalized time is defined as time after beginning-of-charge over time of end-of-discharge. The thick and thin parts of the lines represent the CC and phases, respectively. Same experiment as in Figure 8.

Figure 10 compares the simulation and the experimental results for the highest and lowest C-rates in the same plot. Panel a plots the displacement against charge throughput. Here a hysteresis in the displacement between charge and discharge becomes obvious. Even at 0.05 C where thermal effects are negligible, a hysteresis is visible in the experimental data. This is not reproduced by the simulations. Panel b plots the displacement as function of normalized time. For 0.05 C, we get good quantitative agreement of the results, indicating that the intercalation-induced displacement is predicted correctly. At 10 C, the qualitative shape of the simulated displacement still fits, but there is a discrepancy of almost 10 µm.

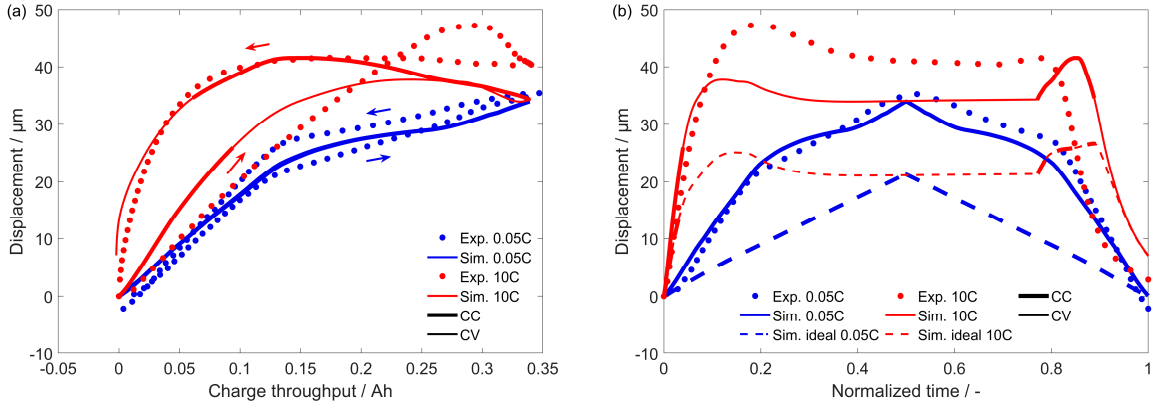

Figure 10. Direct comparison of experimental and simulated displacement for 0.05 C and 10 C, (**a**) as function of charge throughput and (**b**) as function of normalized time. Same data as in Figure 9. In panel (**a**), right-facing arrows indicate the charging phases and left-facing arrows the discharging. In panel (**b**), normalized time is defined as time after beginning-of-charge over time of end-of-discharge. The data sets "Sim. ideal" are simulations with the assumption of ideal solid solution behavior.

For further analysis, we have calculated the MAE for the displacement according to

$$\mathrm{MAE}_{\Delta \mathrm{L}} = \sum_{i=1}^{N} \left| \Delta L_{\mathrm{sim},i} - \Delta L_{\mathrm{exp},i} \right| \tag{23}$$

where the sum runs over one charge and discharge cycle, as for Equation (22). The resulting values for $\mathrm{MAE}_{\Delta \mathrm{L}}$ are 1.95 µm (0.05 C), 2.88 µm (1 C), 3.08 µm (2 C), 5.36 µm (5 C), 8.11 µm (10 C). Again, we see that the error is increasing for higher C-rates. In particular, the deviation of the simulated displacement compared to the experiment is more significant than it is for the voltage and the temperature. When we normalize the MAE to the

measured value range this is even more evident ($NMAE_V$: 7.18% (10 C), MAE_T: 12.85% (10 C), $NMAE_{\Delta L}$: 17.18% (10 C)). This will be discussed in more detail below.

A hysteretic expansion/contraction behavior has been observed before for graphite electrodes [45,68,74,75]. It was explained with different crystallographic pathways during intercalation and deintercalation: During intercalation it is energetically favorable to form discrete stages, whereas during deintercalation it is beneficial to form dilute stages [68,75]. As our model is parameterized with averaged molar volume data of charge and discharge (cf. Table 1), the simulation does not show the hysteretic behavior at 0.05 C. At 10 C the increase in temperature is significantly higher, leading to a significant contribution of thermal expansion. As the temperature peaks are different in magnitude and shape during charging and discharging, the hysteresis effect is pronounced, in agreement between simulation and experiment.

In the simulation, the maximum displacement at the end of charge (Figure 9b, normalized time of approx. 0.5) is independent of the C-rate. This is not the case for the measurements (Figure 9a): There, a shift towards higher maximum displacements with increasing C-rate is evident. This is also clearly visible in Figure 10a (10 C at high charge throughput). This cannot be attributed to temperature, which has cooled back down to ambient level at this point (cf. Figure 8b). A possible explanation for the experimentally-observed behavior is lithium plating, which is known to happen at high currents and also has been reported to happen at room temperature [76]. As plated lithium takes up more volume than intercalated lithium, plating leads to a higher thickness change [77]. Several works have described the visibility of lithium plating in the thickness change of pouch cells [77–81]. The present model does not include plating and is therefore unable to predict the corresponding additional thickness increase. If this is indeed due to lithium plating, and under which C-rates it contributes, has to be subject of future investigations.

Our model uses stoichiometry-dependent partial molar volumes. It is interesting to compare results from simulations using constant partial molar volumes, representing an ideal solid solution. The dashed lines in Figure 10b show simulation results with the assumption of ideal solid solution behavior (cf. Section 3.1). This model shows a linear expansion/contraction behavior at 0.05 C, and clearly smaller overall displacement. This shows clearly that it is necessary to account for the non-ideal behavior of the AM, as it has been stated before by other authors [28,29,50].

4.3. Displacement Components

The P3D model allows to further interpret the simulated displacement in terms of its physical origin, in particular, intercalation-induced swelling versus thermal expansion. To this goal, Figure 11 shows again the simulated displacement of the full cell during the charge-discharge cycles at 0.05 C (left panels) and 10 C (right panels) as function of normalized time (i.e., same datasets as in Figure 10b). The upper panels show a decomposition into the contributions of intercalation-induced displacement ΔL_{int} (blue area) and thermal expansion ΔL_{th} (red area). The two contributions are stacked such that they add up to the total cell displacement (solid black line), thus visualizing the share of each respective component. At 0.05 C thermal expansion is clearly negligible, whereas at 10 C a significant contribution of temperature is obvious. In particular, thermal expansion is responsible for the displacement peaks observed both during charge and discharge. At normalized time ≥ 0.9, where the cell is almost fully discharged but still hot, thermal expansion even dominates the total displacement.

When comparing the simulated cell displacement shown in Figure 3 to the molar volumes of the different AM shown in Figure 2, it is noticeable that the displacement roughly follows to the volume change of graphite (note that in the cell, graphite is cycled between stoichiometric limits X of 0.012 to 0.601), while LCO and NCA have a minor influence. For a quantitative assessment, we have decomposed ΔL_{int} into the contributions of the individual AM. The results are shown in the lower panels of Figure 11. Regardless of the C-rate, one can see the inverse trends of the PE materials LCO and NCA. While

NCA contracts during charge, LCO exhibits an expansion in the same order of magnitude, vice versa during discharge. Furthermore, when comparing the displacement of graphite (solid black line) to the total intercalation-induced displacement (dashed black line), the curves are almost identical. Thus, the opposite expansions of LCO and NCA within the PE compensate each other and the intercalation-induced displacement is almost entirely caused by graphite within the NE.

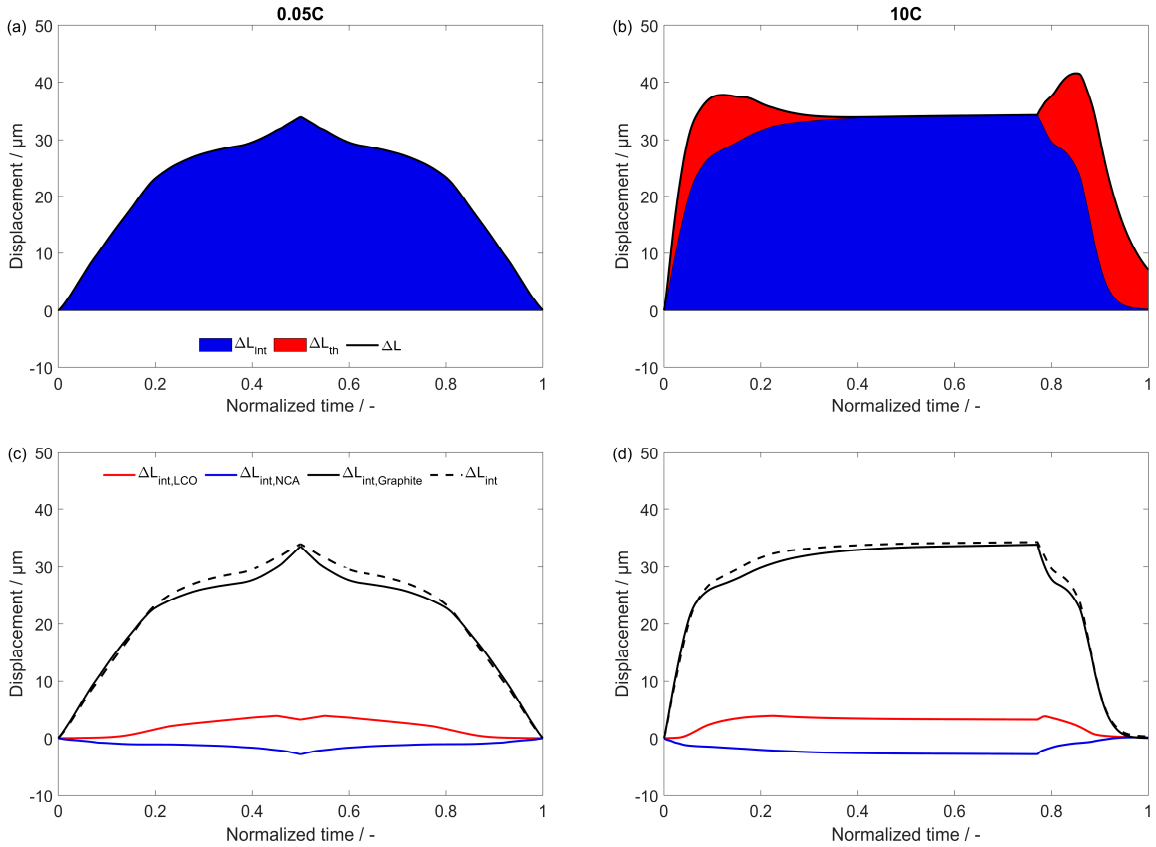

Figure 11. Simulated displacement and its contributions during a charge-discharge cycle. Left panels (**a**), (**c**) at 0.05 C, right panels (**b**), (**d**) at 10 C. The upper panels (**a**), (**b**) show a stacked area plot of the intercalation-induced ΔL_{int} and thermal-induced ΔL_{th} displacement components. The lower panels (**c**), (**d**) show individual contributions of the three AM to the intercalation-induced displacement ΔL_{int}.

Blending of AM is commonly used to tailor the overall electrode performance toward specific requirements [34,82,83]. Our results show that this does not only apply to electrochemical properties, but also to mechanical properties. In combination with the zero-strain NE material lithium titanate (LTO) [50], LCO/NCA blend PE could be used to realize a lithium-ion battery with virtually zero intercalation-induced macroscopic expansion, which might be beneficial regarding cycle life or in applications with confined space requirements.

The present experiment was carried out with a high-power pouch cell under specific thermal boundary conditions (insulating at lower side, convective air cooling at upper side). Both the absolute and the relative thermal displacement contribution can be expected to be different for different cells and boundary conditions. In comparison to high-power cells, a high-energy cell is expected to exhibit higher overpotentials, hence a stronger temperature increase and a higher thermal displacement, if operated at the same C-rate as a high-power cell. However, the thermal boundary conditions are expected to have dominating influence. For example, Carelli et al. [34] clamped the same high-power cell as investigated in the present study in between two aluminum plates. Due to the high thermal conductivity and heat capacity of these plates, the observed temperature increase was <1.5 °C at 10 C (as

compared to >10 °C in the present study). This would result in a proportionally lower thermal expansion.

4.4. Spatial Profiles

The P3D model allows an insight into internal cell states that are not readily accessible experimentally. Figure 12 shows the spatially-resolved strain distribution along the electrode pair (y scale, cf. Figure A1 in the Appendix A) for charging with 0.05 C (only CC charge, panels a and c) and 10 C (CCCV charge, panels b and d). We furthermore compare simulations including thermal expansion (upper panels a and b) to simulations where we switched off thermal expansion ($\alpha_{\mathrm{th}} = 0$, lower panels c and d). Note that the distance values shown on the x axis refer to the fully-discharged cell before cycling (the distance obviously changes during expansion and contraction). For both C-rates it is clearly visible that the major displacement is caused by the graphite NE. At 0.05 C the data with or without thermal expansion look almost identical, because at this low C-rate the temperature stays almost constant. At 10 C there is a clear difference between the simulations with and without thermal expansion. Under the high C-rate, temperature increases much more (cf. Figure 8b), which causes significant thermal expansion. This can especially be seen within the separator region in Figure 12b, as in this model the separator can only expand due to thermal expansion. The strain on the PE is also higher due to additional thermal expansion, however still much smaller than the strain of the NE.

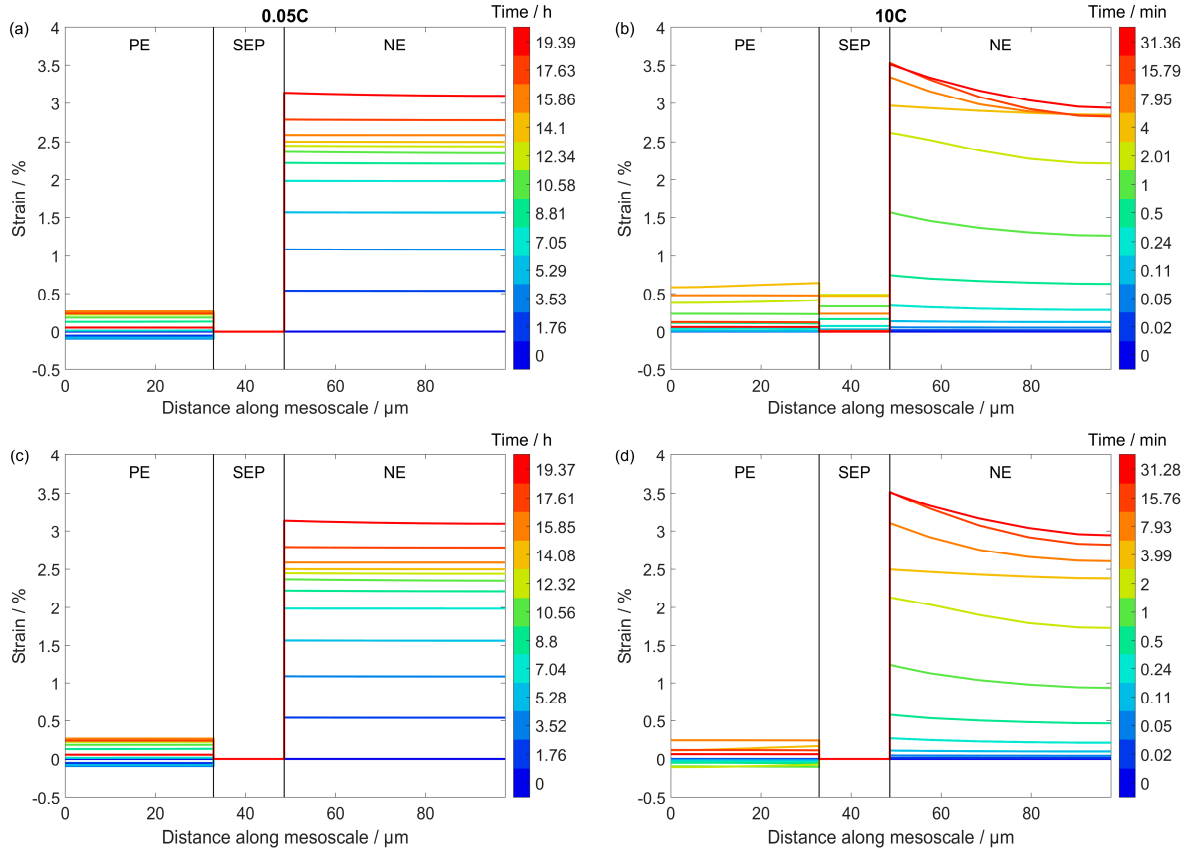

Figure 12. Simulated spatial profiles of the simulated strain distribution along the dimension of the electrode pair (y scale, cf. Figure A1 in the Appendix A) during charging at a rate of (**a**,**c**) 0.05 C and (**b**,**d**) 10 C. The upper panels (**a**,**b**) consider thermal expansion while at the lower panels (**c**,**d**) thermal expansion was switched off. Also note that for 10 C (**b**,**d**) the time steps are displayed in minutes and logarithmically spaced to better resolve the fast progression. Note that only the charge (CCCV) is shown here. SEP, separator.

Another important observation is that there is a visible gradient in the strain distribution across the thickness of the NE. This is caused by a gradient in the stoichiometry of intercalated lithium (in order words, a gradient in local SOC) that arises due to the high current densities, with higher lithium concentrations towards the separator [34]; this effect has been shown to be pronounced in case of thick NEs [39]. Graphite expansion and contraction is known to induce chemical aging due to break-up and re-formation of the solid electrolyte interphase (SEI) [14,84]. Our simulations show that AM particles close to the separator show a larger expansion than those close to the current collector, which likely induces locally inhomogeneous aging.

5. Conclusions and Outlook

In this work we have shown the development and application of a thermo-electro-mechanical model of a lithium-ion battery pouch cell with blend PE. This is an extension of our previously-developed thermo-electrochemical P3D model by including mechanical effects. We considered the non-ideal material-specific volumetric strain of the AM parameterized by literature data of XRD experiments. In order to enable the simulations, we have extended the open-source software Cantera by a thermodynamic model representing intercalation phases with non-ideal molar volumes. A rapid cycling experiment allowed to parameterize both, the effective thermal expansion coefficient and the surface heat transfer coefficient. The effective thermal expansion coefficient for this cell was quantified as $\alpha_{\mathrm{th}} = 9.63{\cdot}10^{-4}\ 1/\mathrm{K}$.

The thermo-electro-mechanical model developed such was used to simulate unconstrained expansion and contraction of the electrodes and the full cell during cycling ("breathing"). We performed both experimental and virtual CCCV charge and discharge cycles at 20 °C ambient temperature over a wide range of C-rates (0.05 C, 1 C, 2 C, 5 C 10 C). We were able to demonstrate a very good agreement between the simulated and the experimental voltage, temperature, and displacement. The model allowed to draw the following conclusions concerning the mechanical behavior of the cell:

- Cell expansion at low C-rates is dominated by intercalation-induced swelling.
- At high C-rates, thermal expansion resulting from electrochemical heating significantly contributes to the cell thickness change, leading to peaks in the displacement vs. time and an increased hysteresis in the displacement vs. charge throughput.
- In the investigated cell, displacement is dominated by the graphite NE. The LCO-NCA blend PE shows almost no displacement due to the opposite expansion behavior of LCO and NCA. These results show that electrode blends can be tailored with respect to their mechanical properties.
- At high C-rates, the expansion shows a significant spatial gradient in the direction along the electrode thickness. This can lead to spatially inhomogeneous electrode aging.

The main advantages of the presented model are: (a) The P3D approach includes all scales relevant for describing the coupled thermo-electro-mechanical coupling in lithium-ion cells; (b) the physicochemical nature of the model allows to describe cell behavior over a broad range of operating conditions; (c) the simulations allow the in-depth analysis of different contributions to cell expansion; (d) because of the underlying homogenization in the three pseudo dimensions, the simulations are computationally efficient.

The model also has a number of weaknesses: (a) The homogenization approach ignores the complexity on the microstructural scale, such as non-spherical particles or particle size distributions, that are likely to affect mechanical behavior; (b) parameterization of the model requires a significant effort (for the present cell we could use a fully-parameterized previous model that only missed the mechanical part); (c) while our model predicts a rate-independent maximum displacement at the end of charge, the experiments clearly show a shift to higher displacements with increasing C-rate. A possible explanation for the experimentally-observed behavior is lithium plating, which is known to happen at high charging currents. We have recently published an electrochemical lithium plating model of the same cell [36]. The present modeling framework is generalized for blend electrodes and

will therefore be able to accommodate plated lithium as NE "blend" component, allowing insight into the contributions of lithium plating to the thickness change. This will be subject of future studies.

Supplementary Materials: The following supporting information can be downloaded at: https://www.mdpi.com/article/10.3390/batteries9070354/s1, Cantera input file.

Author Contributions: Conceptualization, D.S. and W.G.B.; methodology, D.S. and W.G.B.; software, D.S.; validation, D.S.; formal analysis, D.S.; investigation, D.S.; resources, W.G.B.; data curation, D.S.; writing—original draft preparation, D.S.; writing—review and editing, D.S. and W.G.B.; visualization, D.S.; supervision, W.G.B.; project administration, W.G.B.; funding acquisition, W.G.B. All authors have read and agreed to the published version of the manuscript.

Funding: This work was funded by the Deutsche Forschungsgemeinschaft (German Research Foundation, DFG) in the framework of the research training group SiMET—Simulation of Mechanical, Electrical and Thermal effects in Li-ion batteries (281041241/GRK 2218).

Data Availability Statement: The data presented in this study are available on request from the corresponding author.

Conflicts of Interest: The authors declare no conflict of interest.

Appendix A

A short model description and a summary of all model equations and parameters, as well as symbol definitions, are given in this Appendix. With the exception of revisions for the present study, the Appendix is taken from Carelli et al. [85]. A complete description of model development and parametrization is available in the previous works from Carelli et al. [34,36], while the transport equations were derived by Kupper et al. [33].

Appendix A.1. Modeling Domain and Main Assumptions

The model features a pseudo-3D domain (cell scale, electrode pair scale, particle scale), see Figure A1. On the cell level (x scale in Figure A1), heat transport is modeled in one dimension as conduction along the cell thickness, using convective and radiative heat transfer as boundary conditions. This dimension runs perpendicular to the electrode sheets of the pouch cell. On the electrode pair level (y scale in Figure A1), mass and charge transport of Li^+ and PF_6^- ions in the liquid electrolyte and electrons in the solid electrode components is modeled in one dimension along the thickness of the electrode pair. Again, this is perpendicular to the electrode sheet area. For ion transport, we describe species fluxes due to migration and diffusion with a Nernst-Planck approach with concentration- and temperature-dependent diffusion coefficients. Electronic conductivity within the electrodes is assumed high and not rate-limiting. On the particle level (z scale in Figure A1), the diffusion of intercalated lithium atoms in the bulk of the AM particles is modeled using a simple Fickian diffusion approach. The diffusion coefficients are assumed concentration and temperature dependent.

The model framework includes continuity equations for all solid, liquid and gaseous phases present in the electrode, allowing to track formation and growth of new phases. In the continuum setting, all phases are characterized by their respective volume fractions.

The chemical thermodynamics and kinetics are calculated with the Cantera software suite [37]. Details on the use of Cantera for lithium-ion batteries are given by Mayur et al. [47]. All electrochemical reactions are treated within the consistent framework provided by Cantera's *interfaceKinetics* class. For the three AM (LCO, NCA, graphite) we use Cantera's *BinarySolutionTabulatedThermo* class. The electrolyte phase is described through the *IdealSolidSolution* class, for the gas phase we use the *IdealGasPhase* class. All other bulk phases are described using the *StoichSubstance* class. The Cantera input file is provided with this article as supplementary material.

Appendix A.2. Model Equations and Parameters

All model equations are given in Table A1. A list of all symbols used in the tables and in this text is given in Table A2. The model parameters comprise of molar thermodynamic data (Figure A2a–c), solid-state diffusion coefficients (Figure A2d–f), molar volumes (Figure A2g–i), rate coefficients of the electrochemical reactions (Table A3), materials properties of the bulk phases in the electrode pair (Table A4), as well as geometry and transport parameters of the modeling domain at macro-, meso- and microscale (Table A5). The expressions for the ion diffusion coefficients are

$$D_{\mathrm{Li^+}} = 2.06{\cdot}10^{-10}\ \mathrm{m^2 s^{-1}}{\cdot}\exp\left(-\frac{c_{\mathrm{Li^+}}}{1000\ \mathrm{mol\ m^{-3}}}\right){\cdot}\exp\left(-\frac{17.20\ \mathrm{kJ\ mol^{-1}}}{R}\left(\frac{1}{T}-\frac{1}{298\ \mathrm{K}}\right)\right) \quad \text{(A1)}$$

$$D_{\mathrm{PF_6^-}} = 4.81{\cdot}10^{-10}\ \mathrm{m^2 s^{-1}}{\cdot}\exp\left(-\frac{c_{\mathrm{PF_6^-}}}{1000\ \mathrm{mol\ m^{-3}}}\right){\cdot}\exp\left(-\frac{17.20\ \mathrm{kJ\ mol^{-1}}}{R}\left(\frac{1}{T}-\frac{1}{298\ \mathrm{K}}\right)\right) \quad \text{(A2)}$$

Table A1. Model equations.

Macroscale (*x* Direction): Heat Transport in Cell	
Energy conservation	$\rho c_p \frac{\partial T}{\partial t} = \frac{\partial}{\partial x}\left(\lambda \frac{\partial T}{\partial x}\right) + \dot{q}^{\mathrm{V}}$
Heat flux at cell surface	$J_q = \alpha_{\mathrm{surf}}(T - T_{\mathrm{amb}}) + \epsilon\sigma_{\mathrm{SB}}(T^4 - T_{\mathrm{amb}}^4)$
Total heat sources	$\dot{q}^{\mathrm{V}} = \frac{A_{\mathrm{e}}}{V_{\mathrm{cell}}}\left(\int_0^{L_{\mathrm{EP}}} (\dot{q}_{\mathrm{chem}}(y) + \dot{q}_{\mathrm{ohm}}(y))\,\mathrm{d}y + R_{\mathrm{cc}} i^2\right)$
Chemistry heat source	$\dot{q}_{\mathrm{chem}} = \sum_{n=1}^{N_{\mathrm{r}}} \left(r_n A_n^{\mathrm{V}}(-\Delta H_n + F\nu_{\mathrm{e},n}\Delta\phi_n)\right)$
Ohmic heating	$\dot{q}_{\mathrm{ohm}} = \sigma_{\mathrm{elyt}}{\cdot}\left(\frac{\partial \phi_{\mathrm{elyt}}}{\partial y}\right)^2$
Mechanical displacement of complete cell	$\Delta L_{\mathrm{cell}} = N_{\mathrm{EP}}{\cdot}\Delta L_{\mathrm{EP}}$
Mesoscale (*y* direction): Mass and charge transport and mechanics in electrode pair	
Mass conservation of species i	$\frac{\partial(\varepsilon_{\mathrm{elyt}} c_i)}{\partial t} = -\frac{\partial J_i}{\partial y} + \dot{s}_i^{\mathrm{V}} + \dot{s}_{i,\mathrm{DL}}^{\mathrm{V}}$
Charge conservation	$C_{\mathrm{DL}}^{V} \frac{\partial(\Delta\phi)}{\partial t} = \sum_i z_i F \frac{\partial J_i}{\partial y} - i_F^{\mathrm{V}}$
Species fluxes: Nernst-Planck	$J_i = -D_i^{\mathrm{eff}} \frac{\partial c_i}{\partial y} - \frac{z_i F}{RT} c_i D_i^{\mathrm{eff}} \frac{\partial \phi_{\mathrm{elyt}}}{\partial y}$
Mechanical displacement of individual finite volume k	$\Delta L_k = \left(\frac{\sigma_{\mathrm{n}}}{E_k} + \alpha_{\mathrm{th},k}\Delta T + \sum_{j=1}^{N_{\mathrm{AM}}} \varepsilon_{j,k}^0 \cdot \frac{\Delta V_{\mathrm{m},j,k}}{V_{\mathrm{m},j,k}^0}\right) \cdot L_k^0$
Mechanical displacement of electrode pair	$\Delta L_{\mathrm{EP}} = \sum_{k=1}^{N_{\mathrm{FV}}} \Delta L_k$
Microscale (*z* direction): Mass transport in active material particles	
Mass conservation (Fick's 2nd law)	$\frac{\partial c_{\mathrm{Li,AM}}}{\partial t} = \frac{1}{z^2}\frac{\partial}{\partial z}\left(z^2 D_{\mathrm{Li,AM}} \frac{\partial c_{\mathrm{Li,AM}}}{\partial z}\right)$
Chemical kinetics and thermodynamics *	
Interfacial rate of electrochemical reaction n (Butler-Volmer)	$r_n = \frac{i_n^0}{F}\left[\exp\left(\frac{\alpha_{\mathrm{c}} zF}{RT}\eta_{\mathrm{act},n}\right) - \exp\left(-\frac{(1-\alpha_{\mathrm{c}})zF}{RT}\eta_{\mathrm{act},n}\right)\right]$
Exchange current density	$i_n^0 = i_n^{00}{\cdot}\exp\left(-\frac{E_{\mathrm{act},n}}{RT}\right){\cdot}\prod_{i=1}^{N_{\mathrm{R}}}\left(\frac{c_i}{c_i^0}\right)^{(1-\alpha_{\mathrm{c},n})}{\cdot}\prod_{i=1}^{N_{\mathrm{P}}}\left(\frac{c_i}{c_i^0}\right)^{\alpha_{\mathrm{c},n}}$
Overpotential	$\eta_{\mathrm{act},n} = \Delta\phi^{\mathrm{eff}} - \Delta\phi_n^{\mathrm{eq}} = \Delta\phi - R_{\mathrm{SEI}}^{\mathrm{V}} i_{\mathrm{F}}^{\mathrm{V}} - \Delta\phi_n^{\mathrm{eq}}$

Table A1. *Cont.*

Species source terms	$\dot{s}_i^{\mathrm{V}} = \sum_{n=1}^{N_\mathrm{r}} \left(\nu_i r_n A_n^{\mathrm{V}}\right)$
Equilibrium potential (Nernst equation)	$\Delta\phi_n^{\mathrm{eq}} = -\frac{\Delta G_n^0}{zF} - \frac{RT}{zF} \ln\left(\prod_{i=1}^{N_\mathrm{R},N_\mathrm{P}} \left(\frac{c_i}{c_i^0}\right)^{\nu_i}\right)$
Gibbs reaction energy	$\Delta G_n^0 = \sum_{i=1}^{N_\mathrm{R},N_\mathrm{P}} \nu_i \mu_\mathrm{i}^0$
Standard-state chemical potential	$\mu_i^0 = h_i^0 - Ts_i^0 + (p - p_\mathrm{ref})\overline{V}_i$
Current, voltage, potentials	
Cell voltage	$E = \phi_\mathrm{elde,ca} - \phi_\mathrm{elde,an} - i \cdot R_\mathrm{cc}$
Temperature dependence of current collection resistance	$R_\mathrm{cc} = R_\mathrm{cc}^0[1 + \alpha_\mathrm{cc}(T - 293\ \mathrm{K})]$
Cell current	$I_\mathrm{cell} = \frac{A_\mathrm{e}}{V_\mathrm{cell}} \cdot \int_{y=0}^{L_\mathrm{electrode}} \left(i_\mathrm{F}^{\mathrm{V}} + i_\mathrm{DL}^{\mathrm{V}}\right) \mathrm{d}y$
Faradaic current density	$i_\mathrm{F}^{\mathrm{V}} = F\dot{s}_\mathrm{e}^{\mathrm{V}} = \sum_{n=1}^{N_\mathrm{r}} F\left(\nu_{\mathrm{e},n} r_n A_n^{\mathrm{V}}\right)$
Double layer current density	$i_\mathrm{DL}^{\mathrm{V}} = C_\mathrm{DL}^{\mathrm{V}} \frac{\mathrm{d}(\Delta\Phi)}{\mathrm{d}t}$
Species source term from double layer	$\dot{s}_{i,\mathrm{DL}}^{\mathrm{V}} = \frac{z_i}{F} i_\mathrm{DL}^{\mathrm{V}}$ with $i = \mathrm{Li}^+$
Potential step (positive and negative electrode)	$\Delta\phi = \phi_\mathrm{elde} - \phi_\mathrm{elyt}$
Multi-phase management	
Volume fraction of phases	$\frac{\partial\left(\rho_i \varepsilon_j\right)}{\partial t} = \sum_{i=1}^{N_{\mathrm{R},j},N_{\mathrm{P},j}} \dot{s}_i^{V} M_i$
Feedback on transport coefficients (porous electrode theory)	$D_i^\mathrm{eff} = \frac{\varepsilon_\mathrm{elyt}}{{\tau_\mathrm{elyt}}^2} D_i$

* as implemented in Cantera [37,47].

Table A2. List of symbols.

Symbol	Unit	Meaning
A	m^2	Surface area
A_e	m^2	Active electrode area
A_n^{V}	$\mathrm{m}^2 \cdot \mathrm{m}^{-3}$	Volume-specific surface area of reaction n
Bi	1	Biot number
$C_\mathrm{DL}^{\mathrm{V}}$	$\mathrm{F} \cdot \mathrm{m}^{-3}$	Volume-specific double-layer capacity
c_i	$\mathrm{mol} \cdot \mathrm{m}^{-3}$	Concentration of species i in a bulk phase
$c_{\mathrm{max},i}$	$\mathrm{mol} \cdot \mathrm{m}^{-3}$	Maximum concentration of species i in a bulk phase
c_i^0	$\mathrm{mol} \cdot \mathrm{m}^{-3}$	Standard concentration of species i
c_p	$\mathrm{J} \cdot \mathrm{kg}^{-1} \cdot \mathrm{K}^{-1}$	Specific heat capacity
D_i	$\mathrm{m}^2 \cdot \mathrm{s}^{-1}$	Diffusion coefficient of species i
D_i^eff	$\mathrm{m}^2 \cdot \mathrm{s}^{-1}$	Effective diffusion coefficient of species i
E_act	$\mathrm{J} \cdot \mathrm{mol}^{-1}$	Activation energy of forward reaction
E	Pa	Young's modulus
E	V	Cell voltage
F	$\mathrm{C} \cdot \mathrm{mol}^{-1}$	Faraday's constant
ΔH_n	$\mathrm{J} \cdot \mathrm{mol}^{-1}$	Enthalpy of reaction n
h_i^0	$\mathrm{kJ} \cdot \mathrm{mol}^{-1}$	Molar enthalpy of species i

Table A2. *Cont.*

Symbol	Unit	Meaning
ΔG_n^0	$\mathrm{J \cdot mol^{-1}}$	Gibbs energy of reaction n
I_{cell}	A	Cell current
i	1	Index of species
i	$\mathrm{A \cdot m^{-2}}$	Area-specific current (with respect to A_{e})
i^0	$\mathrm{A \cdot m^{-2}}$	Exchange current density
i^{00}	$\mathrm{A \cdot m^{-2}}$	Exchange current density factor
$i_{\mathrm{DL}}^{\mathrm{V}}$	$\mathrm{A \cdot m^{-3}}$	Volume-specific double-layer current
$i_{\mathrm{F}}^{\mathrm{V}}$	$\mathrm{A \cdot m^{-3}}$	Volume-specific faradaic current
j	1	Index of bulk phases
J_{q}	$\mathrm{W \cdot m^{-2}}$	Heat flux from cell surface
J_i	$\mathrm{mol \cdot m^{-2} \cdot s^{-1}}$	Molar flux of species i
k	1	Index of finite volume on y scale
ΔL_k	m	Displacement of finite volume k
ΔL_{cell}	m	Total displacement of complete cell
ΔL_{EP}	m	Total displacement of single electrode pair
ΔL_{int}	m	Intercalation-induced displacement
ΔL_{mech}	m	Mechanical displacement
ΔL_{th}	m	Thermal displacement
L^0	m	Initial length
L_k^0	m	Initial length of finite volume k
L_{EP}	m	Thickness of electrode pair
L	m	Length of thermal conduction
M_i	$\mathrm{kg \cdot mol^{-1}}$	Molar mass of species i
m	kg	Cell mass
n	1	Index of reactions
N_{AM}	1	Number of active materials
N_{FV}	1	Number of compartments on mesoscale
N_{EP}	1	Number of electrode pairs
N_{R}, N_{P}	1	Number of reactants and products in reaction
N_{r}	1	Number of reactions
p	Pa	Pressure
p_{ref}	Pa	Reference pressure
$\dot{q}_{\mathrm{chem}}$	$\mathrm{W \cdot m^{-2}}$	Heat source due to chemical reactions
$\dot{q}_{\mathrm{ohm}}$	$\mathrm{W \cdot m^{-2}}$	Heat source due to ohmic losses
$\dot{q}^{\mathrm{V}}$	$\mathrm{W \cdot m^{-3}}$	Volume-specific heat source
R	$\mathrm{J \cdot K^{-1} \cdot mol^{-1}}$	Ideal gas constant
R_{cc}	$\Omega \cdot \mathrm{m^2}$	Area-specific ohmic resistance of current collection system
R_{cc}^0	$\Omega \cdot \mathrm{m^2}$	Area-specific ohmic resistance of current collection system at reference temperature
$R_{\mathrm{SEI}}^{\mathrm{V}}$	$\Omega \cdot \mathrm{m^3}$	Volume-specific ohmic resistance of SEI film
r_n	$\mathrm{mol \cdot m^{-2} \cdot s^{-1}}$	Interfacial reaction rate of reaction n

Table A2. *Cont.*

Symbol	Unit	Meaning
r_j	m	Particle radius of bulk phase j
s_i^0	$J \cdot mol^{-1} \cdot K^{-1}$	Molar entropy of species i
$\dot{s}_i^V$	$mol \cdot m^{-3} \cdot s^{-1}$	Volumetric species source term
$\dot{s}_{i,DL}^V$	$mol \cdot m^{-3} \cdot s^{-1}$	Volumetric species source term due to double-layer charge/discharge
t	s	Time
ΔT	K	Temperature difference
ΔT_0	K	Initial temperature difference
T	K	Temperature
T_{amb}	K	Ambient temperature (cell surrounding)
T_{surf}	K	Cell surface temperature
V_{cell}	m^3	Volume of cell
$\overline{V}_i$	$m^3 \cdot mol^{-1}$	Partial molar volume of species i
$V_{m,AM}$	$m^3 \cdot mol^{-1}$	Molar volume of active material
$V_{m,i}^*$	$m^3 \cdot mol^{-1}$	Pure species molar volume
$V_{m,AM}^0$	$m^3 \cdot mol^{-1}$	Initial molar volume of active material
$\Delta V_{m,AM}$	$m^3 \cdot mol^{-1}$	Molar volume change of active material
x	m	Spatial position in dimension of battery thickness
X	1	Stoichiometry of lithium in the active material
X_i	1	Mole fraction of species i
SOC	1	State-Of-Charge
y	m	Spatial position in dimension of electrode pair thickness
z	m	Spatial position in dimension of particle thickness
z	1	Number of electrons transferred in charge-transfer reaction
α_{th}	K^{-1}	Thermal expansion coefficient
α_{surf}	$W \cdot m^{-2} \cdot K^{-1}$	Heat transfer coefficient
α_c	1	Cathodic transfer coefficient of electrochemical reaction
α_{cc}	1	Slope of temperature dependent expression of ohmic resistance of current collection system
ϕ_{elde}, ϕ_{elyt}	V	Electric potential in the solid phase and in the electrolyte
$\Delta\phi$	V	Electric potential difference between electrode and electrolyte
$\Delta\phi^{eff}$	V	Effective electric potential difference
$\Delta\phi^{eq}$	V	Equilibrium potential difference
$\Delta\phi_n$	V	Electric potential difference of reaction n
ϵ	1	Emissivity of the cell surface
ε_{AM}^0	1	Initial volume fraction of active material
ε_{elyt}	1	Volume fraction of the electrolyte
ε_{int}	1	Intercalation-induced strain
ε_j	1	Volume fraction of bulk phase j
ε_{mech}	1	Mechanical strain

Table A2. *Cont.*

Symbol	Unit	Meaning
$\varepsilon_{\mathrm{th}}$	1	Thermal strain
η_{act}	V	Activation overpotential
λ	$\mathrm{W{\cdot}m^{-1}{\cdot}K^{-1}}$	Thermal conductivity
μ_i^0	$\mathrm{J{\cdot}mol^{-1}}$	Standard-state chemical potential
$\nu_{\mathrm{e},n}$	1	Stoichiometric coefficient of electron in electrochemical reaction n
ρ	$\mathrm{kg{\cdot}m^{-3}}$	Density
σ_{elyt}	$\mathrm{S{\cdot}m^{-1}}$	Electrolyte conductivity
σ_{n}	Pa	Normal stress
σ_{SB}	$\mathrm{W{\cdot}m^{-2}{\cdot}K^{-4}}$	Stefan-Boltzmann constant
τ_{elyt}	1	Geometric tortuosity of the electrolyte

Table A3. Interfacial chemical reactions and rate coefficients.

No.	Electrode	Reaction	Rate Coefficient	Activation Energy	Symmetry Factor
(1)	Negative	$\mathrm{Li^+[elyt] + e^- + V[C_6] \rightleftarrows Li[C_6]}$	$i^{00} = 8.84{\cdot}10^{14}$ A/m^2 [34]	77.1 kJ/mol [34]	0.5 [34]
(2)	Positive	$\mathrm{Li^+[elyt] + e^- + V[LCO] \rightleftarrows Li[LCO]}$	$i^{00} = 8.20{\cdot}10^{12}$ A/m^2 [34]	72.3 kJ/mol [34]	0.5 [34]
(3)	Positive	$\mathrm{Li^+[elyt] + e^- + V[NCA] \rightleftarrows Li[NCA]}$	$i^{00} = 2.63{\cdot}10^{10}$ A/m^2 [34]	61.0 kJ/mol [34]	0.5 [34]

Table A4. Properties of all bulk phases included in the model.

Layer	Phase	Initial Volume Fraction ε	Density ρ/kg·m^{-3}	Species (Initial Mole Fraction X)
PE	LCO	0.2856	4790	Li[LCO], V[LCO] (depends on SOC)
	NCA	0.2368	3900	Li[NCA], V[NCA] (depends on SOC)
	Electrolyte	0.2976	1270	$C_3H_4O_3$ (0.52), $C_4H_8O_3$ (0.34), Li^+(0.07), PF_6^- (0.07)
	Gas phase	0.030	From ideal gas law	N_2 (1)
	Electron conductor	0.150	2000	No chemically active species
Separator	Separator	0.5	777	No chemically active species
	Electrolyte	0.470	1270	same as at PE
	Gas phase	0.030	From ideal gas law	N_2 (1)
NE	C_6	0.5073	2270	Li[C_6], V[C_6] (depends on SOC)
	Electrolyte	0.4527	1270	same as at PE
	LEDC	0.0008	1300	$(CH_2OCO_2Li)_2$
	Lithium carbonate	0.0092	2100	Li_2CO_3
	Gas phase	0.030	From ideal gas law	N_2 (1)

Table A5. Geometry and transport parameters of the P3D modelling domain.

Parameter	Value
Cell thickness	3 mm
Active electrode area A_{e}	0.02883 m^2
Cell thermal conductivity λ	0.9 W·m^{-1}·K^{-1}
Cell heat capacity c_p	0.95 J·g^{-1}·K^{-1}
Thickness of PE	32.9 µm
Thickness of separator	15.7 µm
Thickness of NE	49.1 µm
Tortuosity of PE τ	1.35

Table A5. *Cont.*

Parameter	Value
Tortuosity of separator τ	1.21
Tortuosity of NE τ	1.22
Diffusion coefficients D_{Li^+} , $D_{PF_6^-}$	See Equations (A1) and (A2)
Specific surface area LCO/electrolyte A^V	$6.67{\cdot}10^5$ m^2/m^3
Specific surface area NCA/electrolyte A^V	$4.28{\cdot}10^6$ m^2/m^3
Specific surface area graphite/electrolyte A^V	2.79 00B7 10^5 m^2/m^3
PE double layer capacitance C_{DL}^V	$1.5{\cdot}10^4$ $F{\cdot}m^{-3}$
NE double layer capacitance C_{DL}^V	$2.8{\cdot}10^5$ $F{\cdot}m^{-3}$
Ohmic resistance of current collection system R_{cc}^0	$7{\cdot}10^{-1}$ $m\Omega{\cdot}m^2$
Slope α_{cc} $(\text{ref.} T = 293\ \text{K})$	-0.01
Electrical conductivity of the SEI layer σ_{SEI}	$1.0{\cdot}10^{-5}$ S/m
Graphite stoichiometry range $X_{Li[C_6]}$ (0 … 100% SOC)	0.012 … 0.601
LCO stoichiometry range $X_{Li[LCO]}$ (0 … 100% SOC)	0.9922 … 0.448
NCA stoichiometry range $X_{Li[NCA]}$ (0 … 100% SOC)	0.790 … 0.186
Radius of LCO particles r_{LCO}	$4.5{\cdot}10^{-6}$m
Diffusion coefficient of Li in LCO $D_{Li,\ LCO}$	See Figure A2d
Radius of NCA particles r_{NCA}	$0.7{\cdot}10^{-6}$m
Diffusion coefficient of Li in NCA $D_{Li,\ NCA}$	See Figure A2e
Radius of graphite particles r_{C_6}	$1.075{\cdot}10^{-5}$m
Diffusion coefficient of Li and graphite D_{Li,C_6}	See Figure A2f

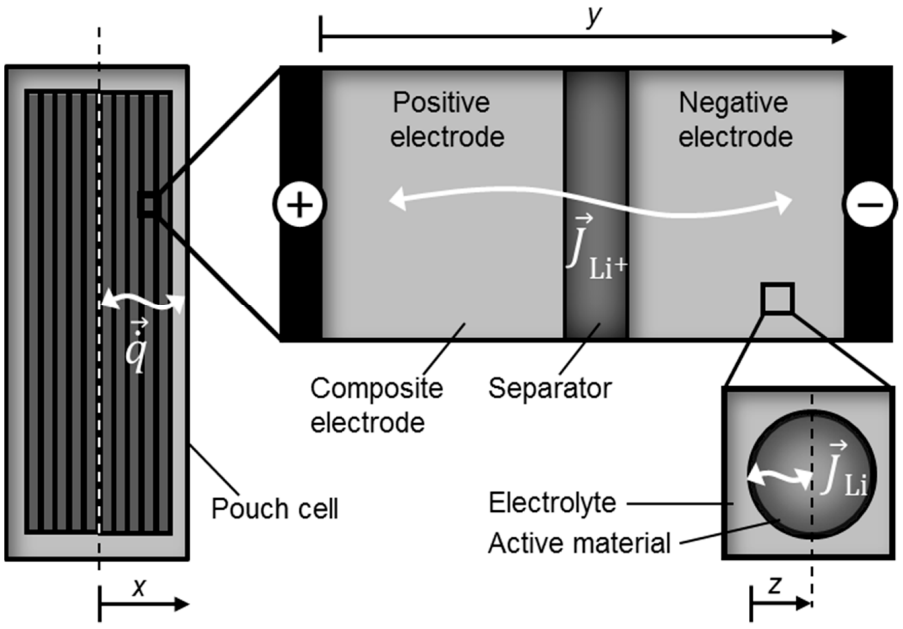

Figure A1. Schematic representation of 1D+1D+1D (pseudo-3D, P3D) modeling domain [36].

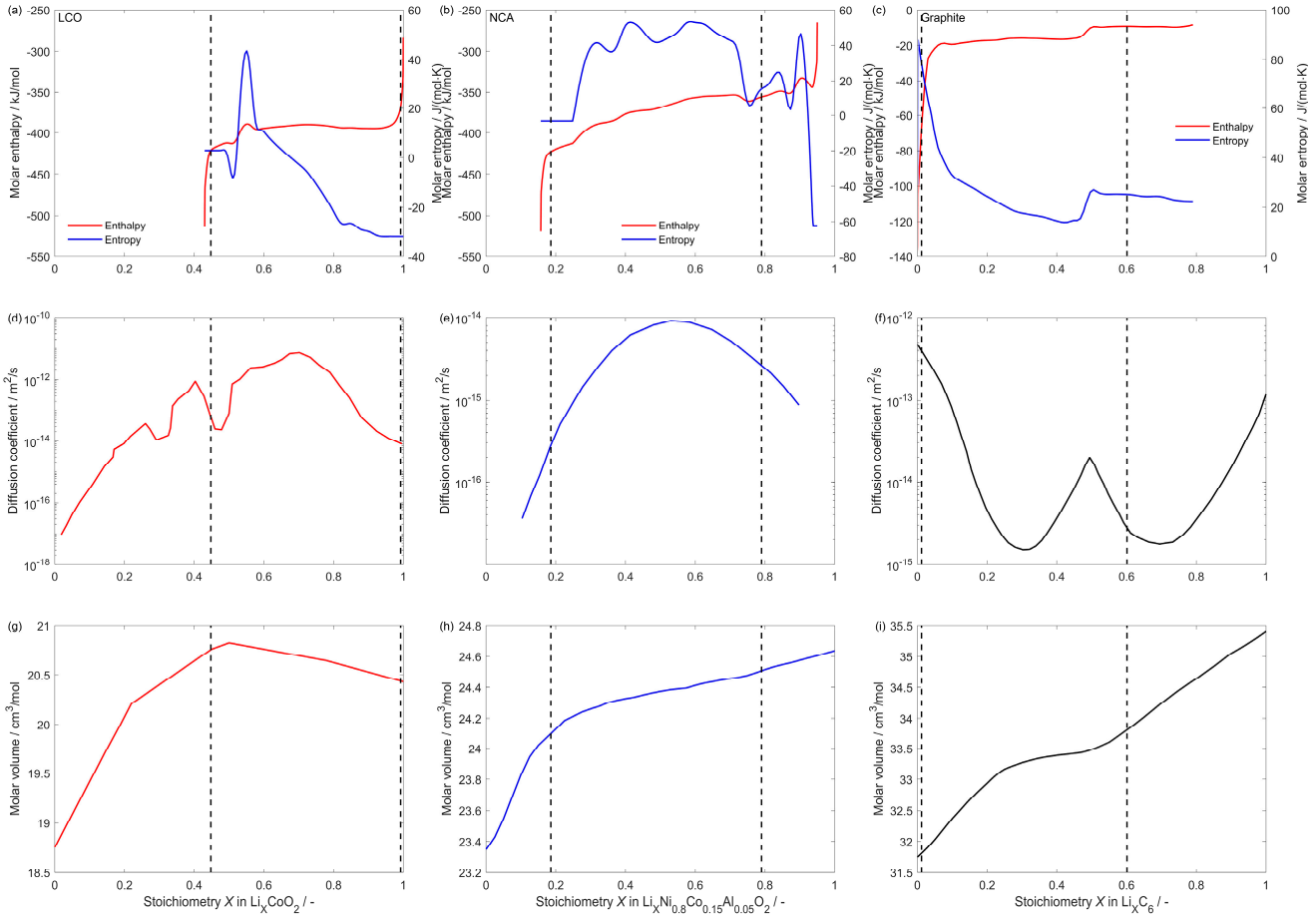

Figure A2. Material data for the three AM (**a**,**d**,**g**) LCO, (**b**,**e**,**h**) NCA and (**c**,**f**,**i**) graphite. The first row (**a**–**c**) shows the molar enthalpies and entropies of intercalated lithium within the three AM. The molar enthalpies and entropies of the vacancies are set to 0 (reference species), see Ref. [47]. The second row (**d**–**f**) shows the solid-state diffusion coefficients of lithium within the three AM at 20 °C. The diffusion is assumed thermally activated with activation energies of 28.95 kJ·mol^{-1}, 115.78 kJ·mol^{-1} and 44.0 kJ·mol^{-1} for LCO, NCA and graphite, respectively. The third row (**g**–**i**) shows the molar volumes as function of lithium stoichiometry of the three AM. The vertical dashed lines indicate the stoichiometry ranges for every AM used in the studied cell within the cut-off voltage limits, as obtained through optimization. See Ref. [34] for details.

References

1. Ziegler, M.S.; Trancik, J.E. Re-examining rates of lithium-ion battery technology improvement and cost decline. *Energy Environ. Sci.* **2021**, *14*, 1635–1651. [CrossRef]
2. Winter, M.; Barnett, B.; Xu, K. Before Li Ion Batteries. *Chem. Rev.* **2018**, *118*, 11433–11456. [CrossRef]
3. Armand, M.; Axmann, P.; Bresser, D.; Copley, M.; Edström, K.; Ekberg, C.; Guyomard, D.; Lestriez, B.; Novák, P.; Petranikova, M.; et al. Lithium-ion batteries—Current state of the art and anticipated developments. *J. Power Sources* **2020**, *479*, 228708. [CrossRef]
4. Birkl, C.R.; Roberts, M.R.; McTurk, E.; Bruce, P.G.; Howey, D.A. Degradation diagnostics for lithium ion cells. *J. Power Sources* **2017**, *341*, 373–386. [CrossRef]
5. Zhao, Y.; Stein, P.; Bai, Y.; Al-Siraj, M.; Yang, Y.; Xu, B.-X. A review on modeling of electro-chemo-mechanics in lithium-ion batteries. *J. Power Sources* **2019**, *413*, 259–283. [CrossRef]
6. Xu, R.; Zhao, K. Electrochemomechanics of Electrodes in Li-Ion Batteries: A Review. *J. Electrochem. Energy Convers. Storage* **2016**, *13*, 652. [CrossRef]
7. Escher, I.; Hahn, M.; Ferrero, G.A.; Adelhelm, P. A Practical Guide for Using Electrochemical Dilatometry as Operando Tool in Battery and Supercapacitor Research. *Energy Technol.* **2022**, *10*, 2101120. [CrossRef]
8. Popp, H.; Koller, M.; Jahn, M.; Bergmann, A. Mechanical methods for state determination of Lithium-Ion secondary batteries: A review. *J. Energy Storage* **2020**, *32*, 101859. [CrossRef]
9. Mendoza, H.; Roberts, S.A.; Brunini, V.E.; Grillet, A.M. Mechanical and Electrochemical Response of a $LiCoO_2$ Cathode using Reconstructed Microstructures. *Electrochim. Acta* **2016**, *190*, 1–15. [CrossRef]

10. Miranda, D.; Costa, C.M.; Lanceros-Mendez, S. Lithium ion rechargeable batteries: State of the art and future needs of microscopic theoretical models and simulations. *J. Electroanal. Chem.* **2015**, *739*, 97–110. [CrossRef]
11. Franco, A.A. Multiscale Modelling and Numerical Simulation of Rechargeable Lithium Ion Batteries: Concepts, Methods and Challenges. *RSC Adv.* **2013**, *3*, 13027–13058. [CrossRef]
12. Krewer, U.; Röder, F.; Harinath, E.; Braatz, R.D.; Bedürftig, B.; Findeisen, R. Review—Dynamic Models of Li-Ion Batteries for Diagnosis and Operation: A Review and Perspective. *J. Electrochem. Soc.* **2018**, *165*, A3656–A3673. [CrossRef]
13. DeCaluwe, S.C.; Weddle, P.J.; Zhu, H.; Colclasure, A.M.; Bessler, W.G.; Jackson, G.S.; Kee, R.J. On the Fundamental and Practical Aspects of Modeling Complex Electrochemical Kinetics and Transport. *J. Electrochem. Soc.* **2018**, *165*, E637–E658. [CrossRef]
14. Kupper, C.; Weißhar, B.; Rißmann, S.; Bessler, W.G. End-of-Life Prediction of a Lithium-Ion Battery Cell Based on Mechanistic Aging Models of the Graphite Electrode. *J. Electrochem. Soc.* **2018**, *165*, A3468–A3480. [CrossRef]
15. Brosa Planella, F.; Ai, W.; Boyce, A.M.; Ghosh, A.; Korotkin, I.; Sahu, S.; Sulzer, V.; Timms, R.; Tranter, T.G.; Zyskin, M.; et al. A continuum of physics-based lithium-ion battery models reviewed. *Prog. Energy* **2022**, *4*, 42003. [CrossRef]
16. Zhang, X.; Shyy, W.; Marie Sastry, A. Numerical Simulation of Intercalation-Induced Stress in Li-Ion Battery Electrode Particles. *J. Electrochem. Soc.* **2007**, *154*, A910–A916. [CrossRef]
17. García, R.E.; Chiang, Y.-M.; Craig Carter, W.; Limthongkul, P.; Bishop, C.M. Microstructural Modeling and Design of Rechargeable Lithium-Ion Batteries. *J. Electrochem. Soc.* **2005**, *152*, A255. [CrossRef]
18. Cheng, Y.-T.; Verbrugge, M.W. Evolution of stress within a spherical insertion electrode particle under potentiostatic and galvanostatic operation. *J. Power Sources* **2009**, *190*, 453–460. [CrossRef]
19. Renganathan, S.; Sikha, G.; Santhanagopalan, S.; White, R.E. Theoretical Analysis of Stresses in a Lithium Ion Cell. *J. Electrochem. Soc.* **2010**, *157*, A155. [CrossRef]
20. Bohn, E.; Eckl, T.; Kamlah, M.; McMeeking, R. A Model for Lithium Diffusion and Stress Generation in an Intercalation Storage Particle with Phase Change. *J. Electrochem. Soc.* **2013**, *160*, A1638–A1652. [CrossRef]
21. Fu, R.; Xiao, M.; Choe, S.-Y. Modeling, validation and analysis of mechanical stress generation and dimension changes of a pouch type high power Li-ion battery. *J. Power Sources* **2013**, *224*, 211–224. [CrossRef]
22. Roberts, S.A.; Brunini, V.E.; Long, K.N.; Grillet, A.M. A Framework for Three-Dimensional Mesoscale Modeling of Anisotropic Swelling and Mechanical Deformation in Lithium-Ion Electrodes. *J. Electrochem. Soc.* **2014**, *161*, F3052–F3059. [CrossRef]
23. Garrick, T.R.; Kanneganti, K.; Huang, X.; Weidner, J.W. Modeling Volume Change due to Intercalation into Porous Electrodes. *J. Electrochem. Soc.* **2014**, *161*, E3297–E3301. [CrossRef]
24. Gomadam, P.M.; Weidner, J.W. Modeling Volume Changes in Porous Electrodes. *J. Electrochem. Soc.* **2006**, *153*, A179. [CrossRef]
25. Rieger, B.; Schlueter, S.; Erhard, S.V.; Jossen, A. Strain Propagation in Lithium-Ion Batteries from the Crystal Structure to the Electrode Level. *J. Electrochem. Soc.* **2016**, *163*, A1595–A1606. [CrossRef]
26. Rieger, B.; Erhard, S.V.; Rumpf, K.; Jossen, A. A New Method to Model the Thickness Change of a Commercial Pouch Cell during Discharge. *J. Electrochem. Soc.* **2016**, *163*, A1566–A1575. [CrossRef]
27. Sauerteig, D.; Hanselmann, N.; Arzberger, A.; Reinshagen, H.; Ivanov, S.; Bund, A. Electrochemical-mechanical coupled modeling and parameterization of swelling and ionic transport in lithium-ion batteries. *J. Power Sources* **2018**, *378*, 235–247. [CrossRef]
28. Ai, W.; Kraft, L.; Sturm, J.; Jossen, A.; Wu, B. Electrochemical Thermal-Mechanical Modelling of Stress Inhomogeneity in Lithium-Ion Pouch Cells. *J. Electrochem. Soc.* **2020**, *167*, 13512. [CrossRef]
29. Pereira, D.J.; Fernandez, M.A.; Streng, K.C.; Hou, X.X.; Gao, X.; Weidner, J.W.; Garrick, T.R. Accounting for Non-Ideal, Lithiation-Based Active Material Volume Change in Mechano-Electrochemical Pouch Cell Simulation. *J. Electrochem. Soc.* **2020**, *167*, 80515. [CrossRef]
30. Zhang, X.; Klinsmann, M.; Chumakov, S.; Li, X.; Kim, S.U.; Metzger, M.; Besli, M.M.; Klein, R.; Linder, C.; Christensen, J. A Modified Electrochemical Model to Account for Mechanical Effects Due to Lithium Intercalation and External Pressure. *J. Electrochem. Soc.* **2021**, *168*, 20533. [CrossRef]
31. Pegel, H.; von Kessel, O.; Heugel, P.; Deich, T.; Tübke, J.; Birke, K.P.; Sauer, D.U. Volume and thickness change of NMC811 | SiO_x-graphite large-format lithium-ion cells: From pouch cell to active material level. *J. Power Sources* **2022**, *537*, 231443. [CrossRef]
32. Clerici, D.; Mocera, F.; Somà, A. Experimental Characterization of Lithium-Ion Cell Strain Using Laser Sensors. *Energies* **2021**, *14*, 6281. [CrossRef]
33. Kupper, C.; Bessler, W.G. Multi-Scale Thermo-Electrochemical Modeling of Performance and Aging of a $LiFePO_4$/Graphite Lithium-Ion Cell. *J. Electrochem. Soc.* **2017**, *164*, A304–A320. [CrossRef]
34. Carelli, S.; Quarti, M.; Yagci, M.C.; Bessler, W.G. Modeling and Experimental Validation of a High-Power Lithium-Ion Pouch Cell with LCO/NCA Blend Cathode. *J. Electrochem. Soc.* **2019**, *166*, A2990–A3003. [CrossRef]
35. Quarti, M.; Bessler, W.G. Model-Based Overpotential Deconvolution, Partial Impedance Spectroscopy, and Sensitivity Analysis of a Lithium-Ion Cell with Blend Cathode. *Energy Technol.* **2021**, *9*, 2001122. [CrossRef]
36. Carelli, S.; Bessler, W.G. Prediction of reversible lithium plating with a pseudo-3D lithium-ion battery model. *J. Electrochem. Soc.* **2020**, *167*, 100515. [CrossRef]
37. Goodwin, D.G.; Moffat, H.K.; Schoegl, I.; Speth, R.L.; Weber, B.W. *Cantera: An Object-oriented Software Toolkit for Chemical Kinetics, Thermodynamics, and Transport Processes*; Zenodo: Genève, Switzerland, 2022. [CrossRef]
38. Mayur, M.; Yagci, M.C.; Carelli, S.; Margulies, P.; Velten, D.; Bessler, W.G. Identification of stoichiometric and microstructural parameters of a lithium-ion cell with blend electrode. *Phys. Chem. Chem. Phys.* **2019**, *21*, 23672–23684. [CrossRef]

39. Quarti, M.; Bayer, A.; Bessler, W.G. Trade-off between energy density and fast-charge capability of lithium-ion batteries: A model-based design study of cells with thick electrodes. *Electrochem. Sci. Adv.* **2023**, *3*, e2100161. [CrossRef]
40. Mohtat, P.; Lee, S.; Siegel, J.B.; Stefanopoulou, A.G. Towards better estimability of electrode-specific state of health: Decoding the cell expansion. *J. Power Sources* **2019**, *427*, 101–111. [CrossRef]
41. Schiffer, Z.J.; Cannarella, J.; Arnold, C.B. Strain Derivatives for Practical Charge Rate Characterization of Lithium Ion Electrodes. *J. Electrochem. Soc.* **2016**, *163*, A427–A433. [CrossRef]
42. Zhang, X.; He, J.; Zhou, J.; Chen, H.; Song, W.; Fang, D. Thickness evolution of commercial Li-ion pouch cells with silicon-based composite anodes and NCA cathodes. *Sci. China Technol. Sci.* **2021**, *64*, 83–90. [CrossRef]
43. Müller, V.; Scurtu, R.-G.; Richter, K.; Waldmann, T.; Memm, M.; Danzer, M.A.; Wohlfahrt-Mehrens, M. Effects of Mechanical Compression on the Aging and the Expansion Behavior of Si/C-Composite | NMC811 in Different Lithium-Ion Battery Cell Formats. *J. Electrochem. Soc.* **2019**, *166*, A3796–A3805. [CrossRef]
44. Oh, K.-Y.; Siegel, J.B.; Secondo, L.; Kim, S.U.; Samad, N.A.; Qin, J.; Anderson, D.; Garikipati, K.; Knobloch, A.; Epureanu, B.I.; et al. Rate dependence of swelling in lithium-ion cells. *J. Power Sources* **2014**, *267*, 197–202. [CrossRef]
45. Rieger, B.; Schlueter, S.; Erhard, S.V.; Schmalz, J.; Reinhart, G.; Jossen, A. Multi-scale investigation of thickness changes in a commercial pouch type lithium-ion battery. *J. Energy Storage* **2016**, *6*, 213–221. [CrossRef]
46. Doyle, M.; Fuller, T.F.; Newman, J. Modeling of Galvanostatic Charge and Discharge of the Lithium/Polymer/Insertion Cell. *J. Electrochem. Soc.* **1993**, *140*, 1526–1533. [CrossRef]
47. Mayur, M.; DeCaluwe, S.C.; Kee, B.L.; Bessler, W.G. Modeling and simulation of the thermodynamics of lithium-ion battery intercalation materials in the open-source software Cantera. *Electrochim. Acta* **2019**, *323*, 134797. [CrossRef]
48. Hetnarski, R.B. *Encyclopedia of Thermal Stresses: With 371 Tables*; Springer: Dordrecht, The Netherlands, 2014; ISBN 978-94-007-2738-0.
49. Rieger, B.; Erhard, S.V.; Kosch, S.; Venator, M.; Rheinfeld, A.; Jossen, A. Multi-Dimensional Modeling of the Influence of Cell Design on Temperature, Displacement and Stress Inhomogeneity in Large-Format Lithium-Ion Cells. *J. Electrochem. Soc.* **2016**, *163*, A3099–A3110. [CrossRef]
50. Koerver, R.; Zhang, W.; de Biasi, L.; Schweidler, S.; Kondrakov, A.O.; Kolling, S.; Brezesinski, T.; Hartmann, P.; Zeier, W.G.; Janek, J. Chemo-mechanical expansion of lithium electrode materials–on the route to mechanically optimized all-solid-state batteries. *Energy Environ. Sci.* **2018**, *11*, 2142–2158. [CrossRef]
51. Deuflhard, P.; Hairer, E.; Zugck, J. One-step and extrapolation methods for differential-algebraic systems. *Numer. Math.* **1987**, *51*, 501–516. [CrossRef]
52. Ehrig, R.; Nowak, U.; Oeverdieck, L.; Deuflhard, P. Advanced Extrapolation Methods for Large Scale Differential Algebraic Problems. In *High Performance Scientific and Engineering Computing*; Lecture Notes in Computational Science and Engineering; Bungartz, H.-J., Durst, F., Zenger, C., Eds.; Springer: Berlin/Heidelberg, Germany, 1999; pp. 233–244.
53. Atkins, P.W.; de Paula, J. *Atkins' Physical Chemistry*, 8th ed.; W.H. Freeman: New York, NY, USA, 2006; ISBN 0-7167-8759-8.
54. Smith, J.M.; van Ness, H.C.; Abbott, M.M.; Swihart, M.T. *Introduction to Chemical Engineering Thermodynamics*, 8th ed.; McGraw-Hill Education: New York, NY, USA, 2018; ISBN 978-1-259-69652-7.
55. Schweidler, S.; de Biasi, L.; Schiele, A.; Hartmann, P.; Brezesinski, T.; Janek, J. Volume Changes of Graphite Anodes Revisited: A Combined Operando X-ray Diffraction and In Situ Pressure Analysis Study. *J. Phys. Chem. C* **2018**, *122*, 8829–8835. [CrossRef]
56. Amatucci, G.G.; Tarascon, J.M.; Klein, L.C. CoO_2, The End Member of the Li_x CoO_2 Solid Solution. *J. Electrochem. Soc.* **1996**, *143*, 1114–1123. [CrossRef]
57. Reimers, J.N.; Dahn, J.R. Electrochemical and In Situ X-Ray Diffraction Studies of Lithium Intercalation in Li_xCoO_2. *J. Electrochem. Soc.* **1992**, *139*, 2091. [CrossRef]
58. Van der Ven, A.; Aydinol, M.K.; Ceder, G.; Kresse, G.; Hafner, J. First-principles investigation of phase stability in Li_xCoO_2. *Phys. Rev. B Condens. Matter* **1998**, *58*, 2975–2987. [CrossRef]
59. Laubach, S.; Laubach, S.; Schmidt, P.C.; Ensling, D.; Schmid, S.; Jaegermann, W.; Thissen, A.; Nikolowski, K.; Ehrenberg, H. Changes in the crystal and electronic structure of LiCoO(2) and LiNiO(2) upon Li intercalation and de-intercalation. *Phys. Chem. Chem. Phys.* **2009**, *11*, 3278–3289. [CrossRef] [PubMed]
60. Winter, M.; Besenhard, J.O.; Spahr, M.E.; Novák, P. Insertion Electrode Materials for Rechargeable Lithium Batteries. *Adv. Mater.* **1998**, *10*, 725–763. [CrossRef]
61. Heng, Y.-L.; Gu, Z.-Y.; Guo, J.-Z.; Wang, X.-T.; Zhao, X.-X.; Wu, X.-L. Research progress on the surface/interface modification of high-voltage lithium oxide cathode materials. *Energy Mater.* **2022**, *2*, 200017. [CrossRef]
62. He, H.; Huang, C.; Luo, C.-W.; Liu, J.-J.; Chao, Z.-S. Dynamic study of Li intercalation into graphite by in situ high energy synchrotron XRD. *Electrochim. Acta* **2013**, *92*, 148–152. [CrossRef]
63. Billaud, D.; Henry, F.X.; Lelaurain, M.; Willmann, P. Revisited structures of dense and dilute stage II lithium-graphite intercalation compounds. *J. Phys. Chem. Solids* **1996**, *57*, 775–781. [CrossRef]
64. Dahn, J.R. Phase diagram of Li_xC_6. *Phys. Rev. B Condens. Matter* **1991**, *44*, 9170–9177. [CrossRef]
65. Dahn, J.R.; Fong, R.; Spoon, M.J. Suppression of staging in lithium-intercalated carbon by disorder in the host. *Phys. Rev. B Condens. Matter* **1990**, *42*, 6424–6432. [CrossRef]
66. Senyshyn, A.; Dolotko, O.; Mühlbauer, M.J.; Nikolowski, K.; Fuess, H.; Ehrenberg, H. Lithium Intercalation into Graphitic Carbons Revisited: Experimental Evidence for Twisted Bilayer Behavior. *J. Electrochem. Soc.* **2013**, *160*, A3198–A3205. [CrossRef]

67. Ohzuku, T.; Iwakoshi, Y.; Sawai, K. Formation of Lithium-Graphite Intercalation Compounds in Nonaqueous Electrolytes and Their Application as a Negative Electrode for a Lithium Ion (Shuttlecock) Cell. *J. Electrochem. Soc.* **1993**, *140*, 2490–2498. [CrossRef]
68. Yazami, R.; Reynier, Y. Thermodynamics and crystal structure anomalies in lithium-intercalated graphite. *J. Power Sources* **2006**, *153*, 312–318. [CrossRef]
69. Takami, N.; Satoh, A.; Hara, M.; Ohsaki, T. Structural and Kinetic Characterization of Lithium Intercalation into Carbon Anodes for Secondary Lithium Batteries. *J. Electrochem. Soc.* **1995**, *142*, 371–379. [CrossRef]
70. Qi, Y.; Guo, H.; Hector, L.G.; Timmons, A. Threefold Increase in the Young's Modulus of Graphite Negative Electrode during Lithium Intercalation. *J. Electrochem. Soc.* **2010**, *157*, A558. [CrossRef]
71. Didier, C.; Pang, W.K.; Guo, Z.; Schmid, S.; Peterson, V.K. Phase Evolution and Intermittent Disorder in Electrochemically Lithiated Graphite Determined Using in Operando Neutron Diffraction. *Chem. Mater.* **2020**, *32*, 2518–2531. [CrossRef]
72. Louli, A.J.; Li, J.; Trussler, S.; Fell, C.R.; Dahn, J.R. Volume, Pressure and Thickness Evolution of Li-Ion Pouch Cells with Silicon-Composite Negative Electrodes. *J. Electrochem. Soc.* **2017**, *164*, A2689–A2696. [CrossRef]
73. Mukhopadhyay, A.; Sheldon, B.W. Deformation and stress in electrode materials for Li-ion batteries. *Prog. Mater. Sci.* **2014**, *63*, 58–116. [CrossRef]
74. Bauer, M.; Wachtler, M.; Stöwe, H.; Persson, J.V.; Danzer, M.A. Understanding the dilation and dilation relaxation behavior of graphite-based lithium-ion cells. *J. Power Sources* **2016**, *317*, 93–102. [CrossRef]
75. Grimsmann, F.; Brauchle, F.; Gerbert, T.; Gruhle, A.; Knipper, M.; Parisi, J. Hysteresis and current dependence of the thickness change of lithium-ion cells with graphite anode. *J. Energy Storage* **2017**, *12*, 132–137. [CrossRef]
76. Waldmann, T.; Kasper, M.; Wohlfahrt-Mehrens, M. Optimization of Charging Strategy by Prevention of Lithium Deposition on Anodes in high-energy Lithium-ion Batteries–Electrochemical Experiments. *Electrochim. Acta* **2015**, *178*, 525–532. [CrossRef]
77. Bitzer, B.; Gruhle, A. A new method for detecting lithium plating by measuring the cell thickness. *J. Power Sources* **2014**, *262*, 297–302. [CrossRef]
78. Rieger, B.; Schuster, S.F.; Erhard, S.V.; Osswald, P.J.; Rheinfeld, A.; Willmann, C.; Jossen, A. Multi-directional laser scanning as innovative method to detect local cell damage during fast charging of lithium-ion cells. *J. Energy Storage* **2016**, *8*, 1–5. [CrossRef]
79. Sturm, J.; Spingler, F.B.; Rieger, B.; Rheinfeld, A.; Jossen, A. Non-Destructive Detection of Local Aging in Lithium-Ion Pouch Cells by Multi-Directional Laser Scanning. *J. Electrochem. Soc.* **2017**, *164*, A1342–A1351. [CrossRef]
80. Spingler, F.B.; Wittmann, W.; Sturm, J.; Rieger, B.; Jossen, A. Optimum fast charging of lithium-ion pouch cells based on local volume expansion criteria. *J. Power Sources* **2018**, *393*, 152–160. [CrossRef]
81. Li, Z.; Fang, R.; Ge, H.; Liu, Z.; Spingler, F.B.; Jossen, A.; Zhang, J.; Liaw, B. Multiphysics Footprint of Li Plating for Li-Ion Battery and Challenges for High-Accuracy Detection. *J. Electrochem. Soc.* **2022**, *169*, 80530. [CrossRef]
82. Chikkannanavar, S.B.; Bernardi, D.M.; Liu, L. A review of blended cathode materials for use in Li-ion batteries. *J. Power Sources* **2014**, *248*, 91–100. [CrossRef]
83. Heubner, C.; Liebmann, T.; Schneider, M.; Michaelis, A. Recent insights into the electrochemical behavior of blended lithium insertion cathodes: A review. *Electrochim. Acta* **2018**, *269*, 745–760. [CrossRef]
84. Laresgoiti, I.; Käbitz, S.; Ecker, M.; Sauer, D.U. Modeling mechanical degradation in lithium ion batteries during cycling: Solid electrolyte interphase fracture. *J. Power Sources* **2015**, *300*, 112–122. [CrossRef]
85. Carelli, S.; Bessler, W.G. Coupling Lithium Plating with SEI Formation in a Pseudo-3D Model: A Comprehensive Approach to Describe Aging in Lithium-Ion Cells. *J. Electrochem. Soc.* **2022**, *169*, 50539. [CrossRef]